



UNIVERSITY OF
CAMBRIDGE

Department of Engineering

Neural Control of Movement

Author Name: Daniel Jackson

Supervisor: Dr Guillaume Hennequin

Date: 26/05/2020

I hereby declare that, except where specifically indicated, the work submitted here-in is my own original work.

Signed Daniel Jackson Date 26/05/2020

ENGINEERING TRIPoS PART IIB

NEURAL CONTROL OF MOVEMENT - TECHNICAL ABSTRACT

Daniel Jackson

Pembroke College

Supervisor: Dr Guillaume Hennequin

In a movement-learning experiment performed by Sadtler et al. (1), 85 neurons in the motor cortex of rhesus macaques were recorded, with a BCI mapping the neural activity to 2-dimensional cursor velocity on a computer screen. After learning to complete the task, the monkeys were required to relearn the desired cursor movements under different perturbations of the BCI.

Sadtler observed that the ability to successfully relearn the movements depended on the geometric location of the BCI, the control space, in the neural space (the vector space defined by the activity of each neuron). They identified a low-dimensional subspace that captured the natural patterns of co-modulation of the neurons, terming it the intrinsic manifold. If the control-space lay within the intrinsic manifold, the monkey learnt to control the cursor as proficiently as before the perturbation; conversely, if the control space lay outside the intrinsic manifold, the monkey was not able to learn the task as successfully as previously.

Hennig et al (2). observed that the neural activity in the null-space of the control-space was not able to vary freely, nor did it follow minimal energy principles according to principles governing muscular redundancy. Instead, they proposed the Fixed Distribution Hypothesis, which states that the variability in output-null activity is constrained by the required output-potent activity. The underlying distribution of firing rates is fixed, and so the distribution of null-space activity is dependent

on the choice of output-potent direction. If the overall distribution is known, one can predict the distribution of output-null activity for any choice of potent directions and any given output-potent activity.

This project uses a network model of dynamics in the motor cortex to simulate the experiment performed by Sadtler in order to investigate why these empirical phenomena arise from the dynamics of the circuit. The neural dynamics and BCI were modelled as a standard state-space control system, to which two types of optimal control in the form of optimal tracking and state LQR were applied. The measure of cost of each method was found to have an inverse relationship with the amount of variance of the neural space accounted for by the BCI. This result explains the observation made by Sadtler; the less well the control space is aligned with the intrinsic manifold, the more energy and consequently the harder it is for the monkey to learn to control the cursor.

In order to investigate Hennig's observation of null-space activity, optimal tracking was used to generate neuron activity, which was then aligned with the output-potent and output null directions. Different methods of generating null-activity were then compared with the true activity, and the KL divergence used to quantify how well they agreed. It was found that using minimum energy principles to model null-space activity did not explain the true activity accurately, while sampling from a multivariate gaussian distribution conditioned on the required output-potent activity fit the true null-space activity most well. This was independent of the choice of mapping used to track the reference signal. We see, therefore, that the fixed distribution hypothesis proposed by Hennig arises naturally from the structural dynamics of the motor cortex.

References

- [1] Sadtler, P., Quick, K., Golub, M. et al. Neural constraints on learning. *Nature* 512, 423–426 (2014).
<https://doi.org/10.1038/nature13665>
- [2] Hennig, J.A., Golub, M.D., Lund, P.J., Sadtler, P.T., Oby, E.R., Quick, K.M., Ryu, S.I., Tyler-Kabara, E.C., Batista, A.P., Byron, M.Y. and Chase, S.M., 2018. Constraints on neural redundancy. *Elife*, 7, p.e36774.

ENGINEERING TRIPOS PART IIB
NEURAL CONTROL OF MOVEMENT - TECHNICAL ABSTRACT

Daniel Jackson
Pembroke College

Supervisor: Dr Guillaume Hennequin

Contents

1	Introduction	6
2	Experimental Set-up	6
2.1	The Intrinsic Manifold	7
2.2	Fixed Distribution	9
3	M1 Cortex Model	11
3.1	Movement Execution	12
3.2	Movement Preparation	14
3.3	Converting to standard form	16
3.4	Calculating the Intrinsic Manifold	16
4	Quantifying conditions for successful task learning	18
4.1	Introduction	18
4.2	Steady State Solution	19
4.3	Optimal Tracking	21
4.3.1	Gaussian Processes	21
4.3.2	Linear Quadratic Integral (LQI) Optimal Control	22
4.3.3	Numerical measurement of error	23
4.4	State LQR	26
4.4.1	Performance Measures	27

4.4.2	Bisection	28
4.5	Discussion	29
4.6	Summary	31
5	Fixed Distribution Hypothesis	31
5.1	Introduction	31
5.2	Tracking a long Gaussian Process	32
5.3	Mapping to output-potent and output-null space	32
5.4	Modelling null-space activity	32
5.4.1	Fixed Distribution Hypothesis	34
5.4.2	Breaking the dependence of null samples on potent activity	36
5.4.3	Minimal Firing Hypothesis	38
5.5	Quantitative Comparison of Distributions	39
5.5.1	KL Divergence of Multivariate Gaussians	39
5.5.2	KL Divergence of the different models of null-space activity	41
5.6	Discussion	41
5.7	Summary	41
6	Conclusion	42
7	Further Work	43
A	Derivation of Lyapunov Equation from Stochastic Differential Equation	44
B	Comparison of different null-space components	44
C	Derivation of KL Divergence of Multivariate Gaussians	47
D	Risk Assessment Retrospective	47

List of Figures

1	Task to be performed by the test subject. The monkey must learn to modulate its neural activity to move a cursor to radially arranged locations. (1)	7
---	--	---

2	Low-dimensional depiction of intrinsic manifold. The intrinsic manifold is shown by the 2-dimensional yellow plane. Starting from an "intuitive control space" (see description in main text), the control space is either re-oriented to lie outside the manifold (blue) or still within the manifold(red). The axes show the firing rates of 3 neurons. (4)	7
3	Task performance success rate across trials for within-manifold perturbation (a) and outside-manifold perturbation (b). Black trace: success rate. Green trace: target acquisition time. Initial trials performed using the intuitive mapping - success rate and acquisition time for consequent trials are relative to the performance under the intuitive mapping. (1)	9
4	Two examples of two redundant activity patterns. (2)	10
5	Low-dimensional depiction of the Fixed Distribution Hypothesis. The output-null activity at any time is conditioned on the required output-potent activity (white dot) (4)	11
6	Recording of neural activity from a monkey during task execution (5)	12
7	Network model of the M1 Cortex with output connected to a two-joint arm model (6)	12
8	Neuron firing rates during movement execution	13
9	Torques applied to two-joint arm model, found by solving the Equation 3 with input firing rates shown in Figure 8	13
10	Two-joint arm model (7)	14
11	Execution of 8 straight reaches	14
12	Geometric visualisation of the optimal subspace. Green: Controlled dynamics. Black: Uncontrolled dynamics ($\mathbf{u}(t) = 0$)	14
13	Convergence of firing rates to the desired initial conditions	15
14	Reaches generated using movement preparation	15
15	Depiction of BCI Model	16
16	Eigenvalues of \mathbf{P}	18
17	Output velocity during optimal constant input, as given by Equation 25.	20
18	Solution Energy $\mathbf{u}^T \mathbf{u}$ plotted against the variance explained by the choice of mapping \mathbf{C} . Red: Combinations of columns from the intrinsic manifold. Black: Mappings consisting of 2 consecutive columns of \mathbf{S} . Green: Random orthonormal mappings	21
19	Two independent gaussian processes	22

20	Left: Step response, Right: Gaussian process tracking. $\lambda_R = 1$	24
21	Left: Step response, Right: Gaussian process tracking. $\lambda_R = 0.1$	24
22	Integral of the instantaneous tracking error under optimal LQI control, $\int e_1^T e_1 dt$ Left: Step input tracking. Right: Gaussian process tracking	25
23	Integral of the augmented tracking error under optimal LQI control, $\int e^T e dt$ Left: Step input tracking. Right: Gaussian process tracking	25
24	Control-input energy, $\int u^T u dt$ Left: Step input tracking. Right: Gaussian process tracking	26
25	Left: LQR State Cost. Right: LQR Control Energy. Black: Consecutive columns of S . Red: Combinations of columns of the intrinsic manifold. Green: Random orthonormal mappings.	28
26	Evolution of LQR control-input energy as λ_R is increased. This is for one particular choice of mapping, C	29
27	Left: LQR State Cost. Right: LQR Control Energy. Black: Consecutive columns of S . Red: Combinations of columns of the intrinsic manifold. Green: Random orthonormal mappings. Blue: Summing increasing numbers of columns of the intrinsic manifold. Bisection performed on the control input energy	30
28	Output-potent components of y	33
29	Black: Samples drawn from a conditional distribution defined by the mean and covariance matrix calculated in Equations 52 and 53. Blue: True samples from tracking activity. This plot shows the top two null components plotted against each other.	34
30	True null-space activity compared with the 2σ contour of the conditional distribution for the top two null components	35
31	Top two components of null activity, with all null components shuffled before assigning to quadrants	36
32	Distribution of shuffled null-space activity, top two components.	37
33	The dashed line shows all redundant activity patterns for the desired output-potent activity. The activity pattern with the lowest energy (orange square) is selected. (2)	38
34	Distribution of first two components of null-space activity according to Minimal Firing Hypothesis	39
35	Top two components of null space activity generated by the minimal firing hypothesis compared with the 2σ contour of the true activity	40

36	KL divergences for each quadrant for different components of null-space activity. Black: Fixed Distribution Hypothesis. Red: Shuffled Null-space components. Green: Minimal Firing Hypothesis	42
37	Second and third true null components	45
38	Second and third shuffled null components	46

1 Introduction

This project seeks to develop further understanding of the applications of Brain-Computer Interfaces (BCIs) as a tool to study learning in the primary motor cortex. Using a BCI allows the experimentalist precise control over the mapping from neural activity to output activity. Measures of task performance can consequently be related to the properties of the mapping and the neural activity.

In this project, a experiment conducted by Sadtler et al.(1) on rhesus macaques will be simulated. The monkeys were required to learn to use motor cortex activity to move a cursor, via a BCI, to targets arranged on a screen. In the experiment, it was observed by Sadtler that the ability of the monkey to learn the task successfully depended strongly on the properties of the BCI. Furthermore, Hennig et al.(2) noted that the distribution of neural activity in the null-space of the BCI was constrained by the required potent activity. These two empirical observations must arise from the dynamics of cortical activity, and so the aim of this project is to show that these two phenomena arise from the dynamics of a network model of the brain.

This report is split into four parts: The first section provides background information to the experiments and describes the two phenomena mentioned above in greater detail. The second develops a simulation of the mon-

key with a BCI performing the task. The third section applies different methods of control to investigate how the choice of BCI affects the ability of the monkey to perform the task, and finally the fourth section considers the distribution of null-space firing rates for some given output-potent activity, investigating the validity of the fixed distribution hypothesis as proposed by Hennig et al.

2 Experimental Set-up

The experiment this project will be simulating was performed as follows. The monkey was restrained in a chair with the activity of 85 neurons in the primary motor cortex being recorded. The activity of the neurons was then mapped to a 2-dimensional output velocity corresponding to a cursor on a computer screen using a brain-computer interface. The task required of the subject was to move the cursor to 8 different targets by modulating the activity of these neurons (Figure 1) Considering the activity of each neuron as one dimension, we can regard the BCI as taking a measurement in an 85-dimensional neural space of activity and mapping it a 2-dimensional output of cursor velocity.

We can consider the BCI mapping as a 2-dimensional control space, and the key feature of this experiment is that the exact location of the this control space within the 85-

dimensional neural space is precisely controlled by the experimentalist. This enables the experimenter to define which activity patterns lead to successful execution of cursor movement and test whether the monkey is able to generate them.

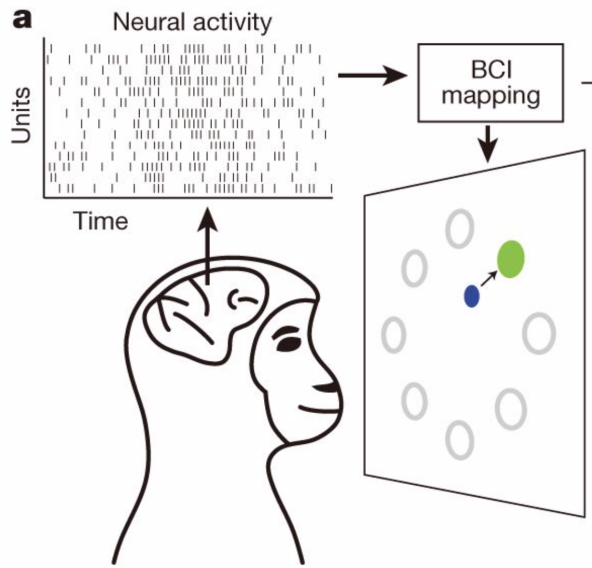


Figure 1: Task to be performed by the test subject. The monkey must learn to modulate its neural activity to move a cursor to radially arranged locations. (1)

2.1 The Intrinsic Manifold

The aim of the experiment performed by Sadtler et al. as described above was to study how easily new patterns of activity were learned when the conditions of the experiment were changed. They first attempted to capture the natural patterns of co-modulation among the recorded neurons. Co-modulation

is the way in which neural units change their activity relative to other neural units - if the activity of one neuron is correlated with the increase in activity of another neuron, these neurons are positively co-modulated. Alternatively, the increase in activity of one neuron can be correlated with the decrease in activity of a second neuron (due to, for example, an inhibitory connection), in which case these neurons are negatively co-modulated. They found that the neural activity could be accurately described by a low-dimensional sub-space that they termed the intrinsic manifold. Figure 2 shows, as an example, a 2-dimensional intrinsic manifold in the 3-dimensional neural space.

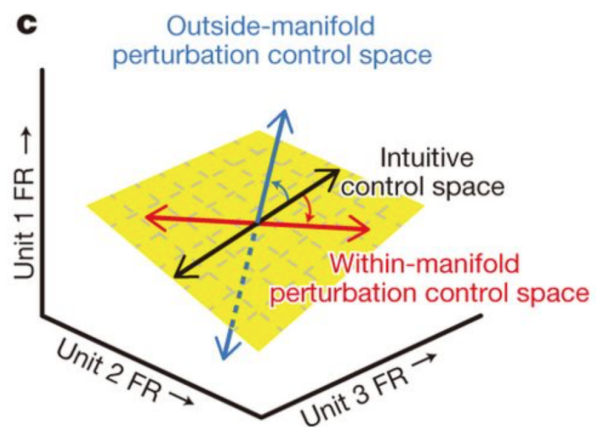


Figure 2: Low-dimensional depiction of intrinsic manifold. The intrinsic manifold is shown by the 2-dimensional yellow plane. Starting from an "intuitive control space" (see description in main text), the control space is either re-oriented to lie outside the manifold (blue) or still within the manifold (red). The axes show the firing rates of 3 neurons. (4)

At the start of each day, a calibration set of trials was performed to define an intuitive control space, with which the subject had proficient control over the cursor. (Figure 2, black line). By definition, the intuitive control space lies within the intrinsic manifold. The level of task-performance achieved using the intuitive mapping was used as the baseline to which all other performances were compared. The BCI mapping was then changed such that the control space lay either within (Figure 2, red line), or outside (Figure 2, blue line), the intrinsic manifold.

If the mapping is perturbed but remains within the intrinsic manifold, the monkey simply needs to learn a new relationship between the co-modulation patterns and cursor movement, however the co-modulation patterns themselves do not change. In contrast, to learn an outside-manifold perturbation, the monkey would have to alter the way in which the neural units contributed to co-modulation patterns, as the current patterns can only easily generate activity in the intrinsic manifold. In both cases the test subjects had to undergo learning to regain accurate control of the cursor, however under a within-manifold perturbation, the subjects simply had to learn the new relationship between the natural co-modulation patterns and the cursor movement in order to regain accurate control. To restore proficient control of the cursor under an outside-manifold perturbation, the subjects had to learn to generate completely new pat-

terns co-modulation, rather than using the natural ones.

As expected, after the perturbed mappings were introduced, the task completion rate was immediately reduced. In the case of within-manifold perturbations, the success-rate soon increased to the level of the intuitive mapping (Figure 3a), and the time taken to perform the movement decreased, indicating that the subjects had managed to learn to control the cursor quickly and accurately, indicating that they had learnt the relationship between the cursor movement and their co-modulation patterns. For outside-manifold perturbations however, the task performance, while showing some initial improvement, remained significantly lower than under the intuitive mapping (Figure 3b), suggesting that there is a limit to how well the current co-modulation patterns are able to generate the required activity, and that learning to create new co-modulation patterns is not possible. Furthermore, when the intuitive mapping was reinstated, the subject's task performance returned to the original levels, confirming the hypothesis that no learning had taken place. In comparison, when the intuitive mapping was presented after a within-manifold perturbation had been applied, the subject initially failed to perform the task successfully and had to relearn the intuitive mapping, confirming that the perturbed mapping had been learnt. The conclusion that Sadtler et al. came to was that the patterns of co-modulation are strongly dependent on

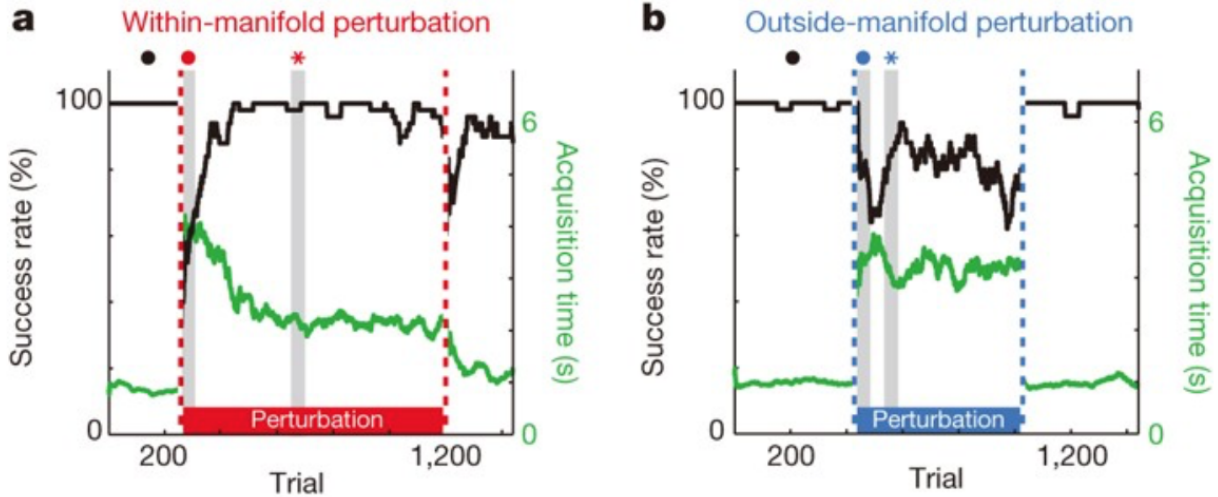


Figure 3: Task performance success rate across trials for within-manifold perturbation (a) and outside-manifold perturbation (b). Black trace: success rate. Green trace: target acquisition time. Initial trials performed using the intuitive mapping - success rate and acquisition time for consequent trials are relative to the performance under the intuitive mapping. (1)

the structure of the network of neurons in M1. Learning can alter the association between co-modulation and cursor movement, however the subject cannot change the structure of the underlying network and generate new patterns of co-modulation.

2.2 Fixed Distribution

The dimensionality reduction from 85 dimensions of neural activity to 2 dimensions of output velocity means that the same output activity can be generated by many different combinations of neural activity. This is termed neural redundancy. In muscle activity, for example, a small number of muscles are driven by many neurons, so many different patterns of neural activity must be able to achieve the

same movement. A corollary of this is the presence of a neural output-potent space and an output-null space. As long as the activity in the output-potent space is performing the required task, the neural activity can vary freely in the null-space, as any activity will not be read-out in the output. Neural redundancy can thus offer many computational benefits, for example allowing the preparation of a movement using activity in the null-space without executing the movement (3). By studying the structure of neural activity in the null-space, Hennig et al. sought to determine whether there were any constraints that limited the selection of activity patterns generated. If such constraints existed, it would suggest that the extent to which redundancy can be exploited by the brain for computation

is limited.

When recording from the brain, the experimentalist does not know how exactly neural activity affects neurons or muscles downstream, so studying neural redundancy can be difficult, as it is impossible to identify which activity is redundant. The benefit of using a BCI to study neural redundancy is that the division into potent and null activity is precisely known, as the location of the control-space is set by the experimentalist. A low-dimensional example of this decomposition is shown in Figure 4, where the activity of two neurons controls the velocity of a cursor in one dimension. The two dark green activity patterns produce one cursor movement, while the two light green patterns produce a different movement. We see that any population activity pattern can be decomposed into two orthogonal components: output-potent activity and output-null activity. The output-potent component determines the cursor's movement, whereas the output-null component has no effect on the cursor. Two activity patterns are redundant if they different output-null activity, but the same output-potent activity.

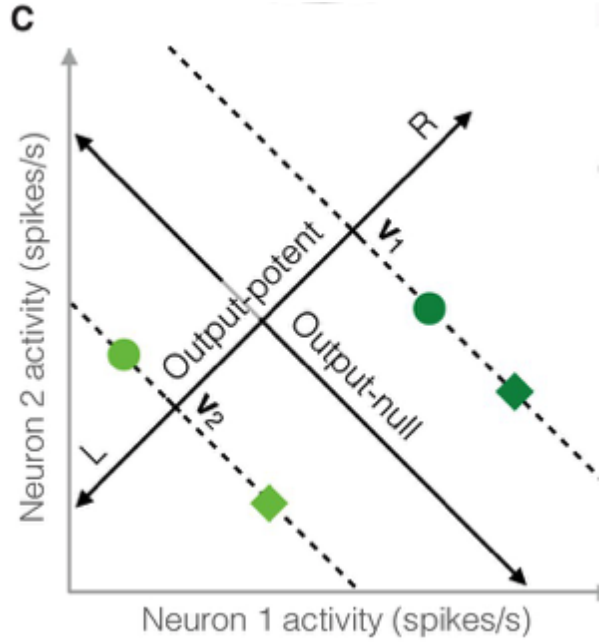


Figure 4: Two examples of two redundant activity patterns. (2)

Hennig et al. compared several hypotheses for how the redundant activity patterns were being generated and compared them with the measured activity gathered during the experiment. They found that the model that best fit the data suggested that the distribution of activity in output-null dimensions was coupled with the activity in output-potent dimensions, even when the BCI mapping was changed. For a given output-potent activity, the distribution of the corresponding output-null activity remained the same as it was under a different BCI mapping, even if this activity was not output-null under the previous mapping. Consequently, this means that one cannot view the output-null space as a space in which neural activity can evolve unconstrained. Instead,

the distribution of output-null activity is conditional on the corresponding output-potent activity. Performing a task successfully fixes the required output-potent activity, and so the variations in output-null activity are constrained too. Hennig et al. termed this model the 'Fixed Distribution Hypothesis'. This is depicted in Figure 5. The underlying distribution of firing rates is fixed, and so the distribution of null-space activity is dependent on the choice of output-potent direction. If the distribution is known, one can predict the structure of output-null activity for any choice of potent directions.

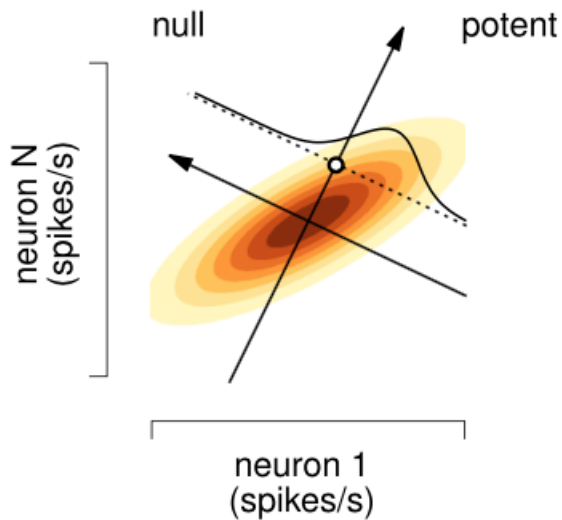


Figure 5: Low-dimensional depiction of the Fixed Distribution Hypothesis. The output-null activity at any time is conditioned on the required output-potent activity (white dot) (4)

A commentary by Kao and Hennequin (4) explains how this result might arise as a conse-

quence of the internal structure of M1. Consider a model of cortical dynamics consisting of populations of inhibitory and excitatory neurons. In order to perform the task successfully, both populations must receive inputs optimized to produce desired activity in some chosen potent direction. The presence of strong network interactions means that the activity is naturally steered along some "preferred directions" further than it is along others, due to the fact that the network preferentially produces correlated activity patterns. Under optimal control, this gives rise to a "fixed distribution" that constrains the repertoire of activity able to be produced by M1. This repertoire is completely independent of the specific potent directions chosen by the experimentalist, as it is purely an artefact of the network's intrinsic dynamics. We see, therefore, that the fixed distribution hypothesis proposed by Hennig et al. arises naturally from the structure of M1.

3 M1 Cortex Model

It is thought that monkeys use their ability to use M1 activity to prepare for to drive the BCI in the experiment performed by Sadtler. While the monkeys were restrained at the start of the experiment, after learning had taken place these restraints could be loosened, such that they could move their hands. However, it was observed that no movement was taking place,

despite recordings showing activity in the motor cortex.

Figure 6 shows the recording of neural activity from a monkey actively moving its arm. We see that the first phase is a preparatory phase before the activity that drives the movement takes over. During preparation, muscles are receiving signals, however no movement is taking place, so this suggests that the activity must be occurring in the null-space of the mapping from neural activity to muscle activity (3)

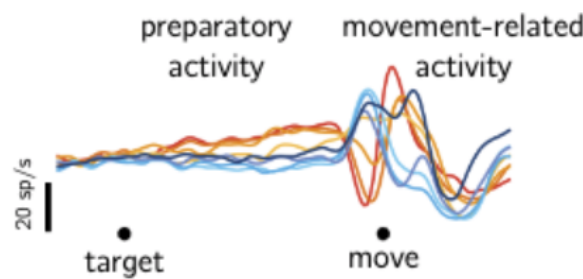


Figure 6: Recording of neural activity from a monkey during task execution (5)

The monkeys initially weren't able to move their hands, and so had to learn to actuate the cursor by only using preparatory activity. This may lie in the null-space of the mapping to muscle activity, but it can lie in the output-potent space of the mapping to cursor velocity as that mapping is set by the experimenter.

Consequently, in order to simulate BCI dynamics, we must first construct a model of movement preparation in the M1 cortex. The model described in this section was developed

by Kao et al. (6), with the parameters of the model provided to me. The process followed by Kao to generate straight reaches will be recreated, starting with movement execution without preparation, before incorporating the preparatory phase, to ensure that the model works as expected. Once we have a working model of movement preparation, the movement execution phase can be removed and a BCI used instead to map the preparatory activity to cursor velocity, at which point the phenomena described in Sections 2.1 and 2.2 can be investigated.

3.1 Movement Execution

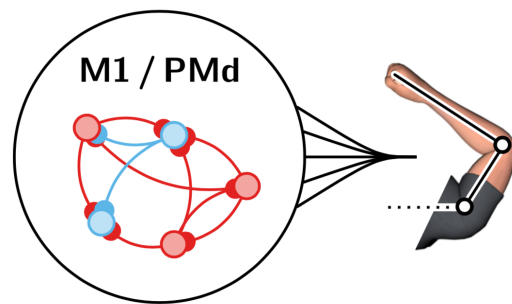


Figure 7: Network model of the M1 Cortex with output connected to a two-joint arm model (6)

Figure 7 shows an inhibition stabilised network with $N_E = 160$ excitatory neurons and $N_I = 40$ inhibitory neurons. The output maps to a 2-joint arm model (Li and Todorov (7)). The vector $x(t)$ of neural activity is described by

the non-linear first-order ODE:

$$\tau \frac{dx}{dt} = -x(t) + W\phi[x(t)] + \bar{h} + \dots \quad (1)$$

where $\tau = 150$ ms is the single-neuron time constant, W is the synaptic connectivity matrix, and $\phi(x_i) = \max(x_i, 0)$ is the relu non-linearity that converts the neuronal activation into firing rates and \bar{h} is a constant input.

The output of Equation 1 is mapped to input torques to the arm model by:

$$m(t) = C\phi[x_E(t)] \quad (2)$$

with $C \in \mathbb{R}^{2 \times N_E}$. Given the synaptic connective matrix and the set of initial conditions, a numerical Euler method was used to solve Equation 1 for $x(t)$, shown in Figure 8. The evolution of torques output by Equation 2 with the firing rates input is shown in Figure 9.

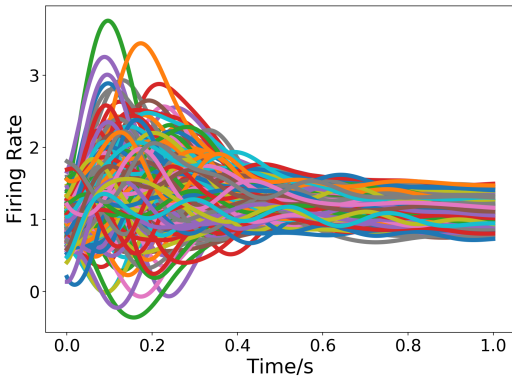


Figure 8: Neuron firing rates during movement execution

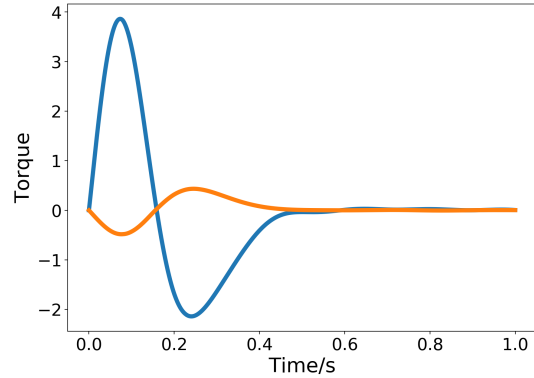


Figure 9: Torques applied to two-joint arm model, found by solving the Equation 3 with input firing rates shown in Figure 8

These torques are used as inputs for the arm model shown in Figure 10, which is described by angles θ_1 and θ_2 obeying:

$$m(t) = M(\theta)\ddot{\theta} + C(\theta, \dot{\theta}) + B\dot{\theta} \quad (3)$$

with $M(\theta)\ddot{\theta}$, $C(\theta, \dot{\theta})$ and B as defined in (6). This was solved by first converting into the standard form system of first order ODEs and then applying the same Euler equation solver. The 8 sets of initial conditions give 8 straight reaches, shown in Figure 11. This demonstrates that given a correct set of initial conditions, the model generates the desired set of reaches.

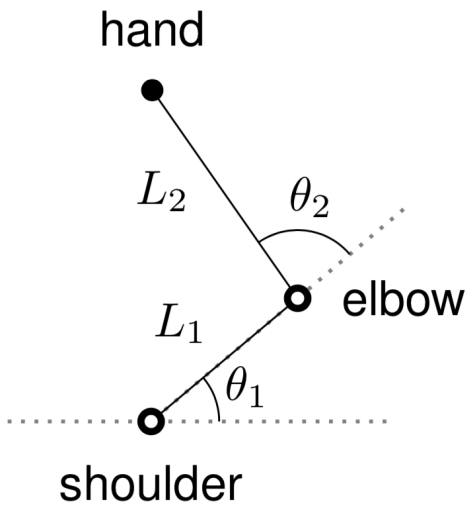


Figure 10: Two-joint arm model (7)

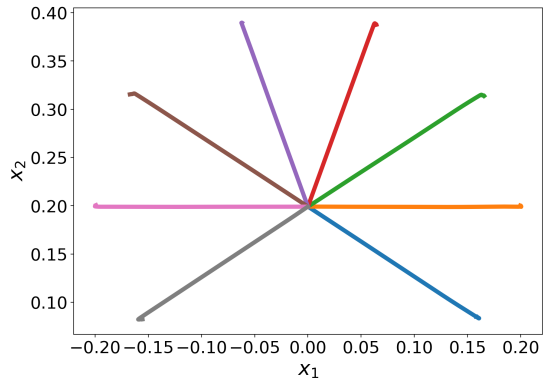


Figure 11: Execution of 8 straight reaches

3.2 Movement Preparation

Now to this model of movement execution we add the process of movement preparation. In the high-dimensional neural space, one can define a subspace termed the 'optimal subspace' (Figure 12), which describes the set of initial conditions that causes the movement to ex-

ecute as desired. The role of the preparatory activity is to move the neural activity from some spontaneous activity into the optimal subspace, at which point the control input is withdrawn and the movement is initiated.

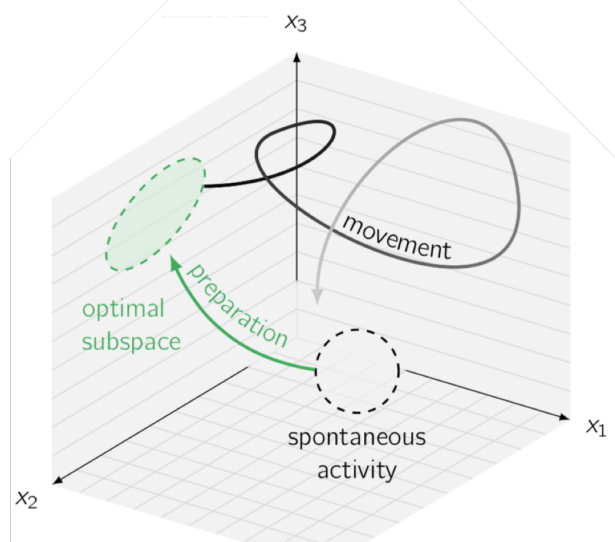


Figure 12: Geometric visualisation of the optimal subspace. Green: Controlled dynamics. Black: Uncontrolled dynamics ($\mathbf{u}(t) = 0$)

This is achieved by introducing a preparatory control input variable $\mathbf{u}(t)$:

$$\tau \frac{d\mathbf{x}}{dt} = -\mathbf{x}(t) + \mathbf{W}\phi[\mathbf{x}(t)] + \mathbf{h} + \mathbf{u}(t) + \dots \quad (4)$$

During preparation, this acts as a feedback loop to bring the neural activity into the optimal subspace. \mathbf{u} is then removed and the network evolves autonomously, executing the movement as described in the previous section. The optimal controller $\mathbf{u}(t)$ consists of:

$$\mathbf{u}(t) = \tilde{\mathbf{u}} + \mathbf{K}\phi[\mathbf{x}(t)] \quad (5)$$

where $\tilde{\mathbf{u}}$ is a movement specific steady input, and $\mathbf{K}\phi[\mathbf{x}(t)]$ is the optimal feedback con-

troller. \mathbf{K} is defined as $\lambda^{-1}\mathbf{P}$ where \mathbf{P} is the solution to the Riccati Equation:

$$\mathbf{A}^T \mathbf{P} + \mathbf{P} \mathbf{A} - \lambda^{-1} \mathbf{P} \mathbf{P} + \mathbf{Q} = 0 \quad (6)$$

and \mathbf{A} is the effective state transition matrix $\mathbf{A} = \mathbf{W} - \mathbf{I}$. \mathbf{Q} is found by solving the Lyapunov Equation:

$$\mathbf{A}^T \mathbf{Q} + \mathbf{Q} \mathbf{A} + \tau \mathbf{C}^T \mathbf{C} = 0 \quad (7)$$

We calculate $\tilde{\mathbf{u}}$ by requiring \mathbf{x} to reach initial condition \mathbf{x}^* , so the control input must eventually settle at a steady-state value given by:

$$0 = -\mathbf{x}^* + \mathbf{W} \mathbf{x}^* + \tilde{\mathbf{u}} + \mathbf{K} \mathbf{x}^* + \mathbf{h}$$

$$\tilde{\mathbf{u}} = -(\mathbf{W} - \mathbf{I} + \mathbf{K}) \mathbf{x}^* - \mathbf{h}$$

Initialising \mathbf{x} at the spontaneous firing rate and solving Equation 4 causes the firing rates to evolve as shown in Figure 13. We see that after initial transience the firing rates converge to a steady value. We can now remove the control input and use this steady state value as the initial conditions for the movement execution described in the previous section. The reaches shown in Figure 14 confirm that the correct set of initial conditions has been reached.

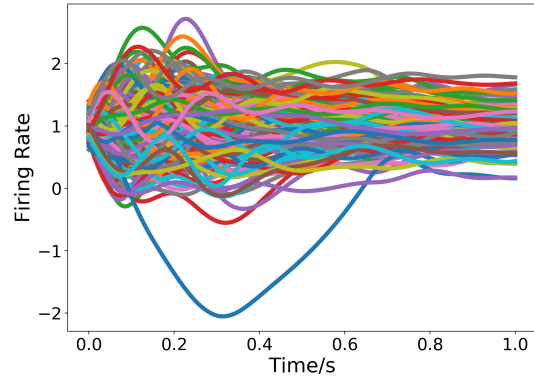


Figure 13: Convergence of firing rates to the desired initial conditions

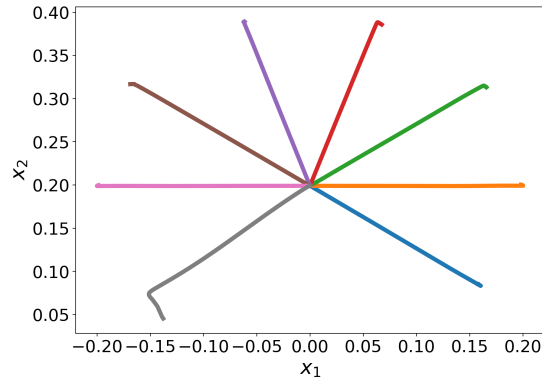


Figure 14: Reaches generated using movement preparation

This confirms that the model of movement preparation functions correctly. We now use this to model the BCI. Consider the model depicted in Figure 15. The subject has learned a repertoire of 8 $\tilde{\mathbf{u}}$ which we term neural coding units. To execute a movement, the subject activates one of these units, which inputs the corresponding $\tilde{\mathbf{u}}$ into the dynamics, with \mathbf{W} and \mathbf{K} ensuring that the activity converges to

the optimal subspace. This preparatory activity is mapped to cursor velocity by the BCI, C . We can now change the mapping C . The location of the control space (which represents the BCI) within the neural space can now be altered in order to investigate how the test subjects use the repertoire of neural coding units they already have to learn to generate a new set of velocities. We can write this in equation form by collating all of the learnt initial conditions \tilde{u} into one matrix, \tilde{U} . Assuming that the subject cannot change the structure of M1, the synaptic connectivity matrix W is constant, thus the subject is internally constrained to using a linear combination of the columns of \tilde{U} , given by $\tilde{U}z$, as input to the M1 network in order to generate the correct cursor movement:

$$\dot{x} = -x + (W + K)\phi[x] + \tilde{U}z + \bar{h} \quad (8)$$

From the experiment performed by Sadtler, we expect to be able to generate a new set of initial conditions from the old if we choose a mapping that is within the intrinsic manifold, and we expect not to be able to adapt if the new mapping is not within the intrinsic manifold.

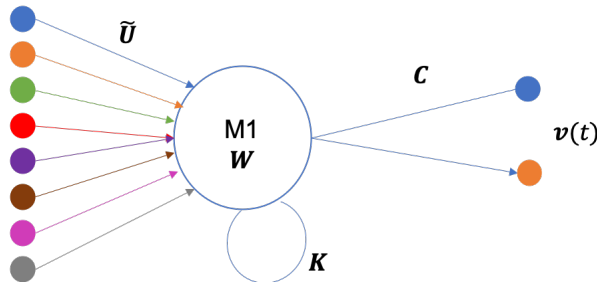


Figure 15: Depiction of BCI Model

3.3 Converting to standard form

The presence of the relu non-linearity $\phi[\cdot]$ means that Equation 8 is a non-linear differential equation. These are considerably harder to analyse, and so for the sake of simplicity, we will remove the non-linearity, writing

$$\dot{x} = (W - I + K)x + \tilde{U}z + \bar{h} \quad (9)$$

The relu function takes any negative value and outputs 0. Considering Figure 13, we see that very few of the neurons ever have negative firing rates, so removing the relu function will make very little difference to the output. We would also like to re-write the dynamics in standard state-space form, such that:

$$\dot{x} = Ax + Bu + \bar{h} \quad (10)$$

Comparing the two, we then define $(W - I + K) \triangleq A$, and rename $\tilde{U} = B$ and $z = u$. This state-space form will be the basis of future analysis.

3.4 Calculating the Intrinsic Manifold

The intrinsic manifold captures the natural patterns of co-modulation of the recorded neurons. One way to find it is by first solving the following stochastic differential equation (SDE):

$$dx = Axdt + BdW \quad (11)$$

Spatially and temporally uncorrelated white noise dW is being input into the 8 input channels concurrently, driving the system. The noise enters the M1, and reverberates due to the effect of the \mathbf{A} matrix. The system will eventually reach a some statistical steady state, with \mathbf{x} fluctuating, driven by the noise. The dynamics means there is short-term memory, so the fluctuations in \mathbf{x} will no longer be white in time, but will have some temporal correlation length (although it will still look noisy). We can then find the covariance matrix, where the ij^{th} element tells us the covariance between the fluctuations in neuron j and neuron i . This covariance matrix also obeys the following Lyapunov equation (see Appendix A):

$$\mathbf{AP} + \mathbf{PA}^T + \mathbf{BB}^T = 0 \quad (12)$$

where the matrix $\mathbf{P} = \mathbb{E}[\mathbf{x}(t)\mathbf{x}(t)^T]$ is precisely the covariance matrix of the stochastic differential equation. We can thus find \mathbf{P} either algebraically by simulating the stochastic differential equation and taking the covariance or analytically by solving the Lyapunov equation.

We find the intrinsic manifold by performing PCA on the covariance matrix. The intrinsic manifold is then given by the axes of largest fluctuations. We find the eigenvalues and eigenvectors of \mathbf{P} , where the meaning of each eigenvalue is the amount of variance that is captured in the corresponding eigenvector. Denote the orthonormal matrix of eigenvec-

tors as \mathbf{S} , where the first column corresponds to the maximum eigenvalue. The top few non-zero eigenvalues thus define the intrinsic manifold, with their respective columns of \mathbf{S} defining the directions in state space where there are variations of activity due to the white noise inputs.

Figure 16 shows the eigenvalues of \mathbf{P} plotted in descending order. As the length of time the SDE is simulated for increases, the eigenvalues of the covariance of the activity generated will converge to the solution from the Lyapunov equation. We see that they quickly decrease in magnitude, tending towards 0. To define the intrinsic manifold, we quantify the amount of variance accounted for by the columns of \mathbf{S} :

$$V = \text{trace}(\mathbf{S}_{0...i} \mathbf{PS}_{0...i}^T) \quad (13)$$

where $\mathbf{S}_{0...i}$ represents the first i columns of \mathbf{S} and \mathbf{P} is the covariance matrix of the spontaneous activity. As i increases, more of the total variance of \mathbf{S} is accounted for, although more and more slowly, as the variance accounted for by each consecutive eigenvector decreases (see Figure 16). Requiring the intrinsic manifold to account for 95% of the total variance, we find that this occurs using the first 21 columns of \mathbf{S} . These 21 orthonormal columns thus define the intrinsic manifold.

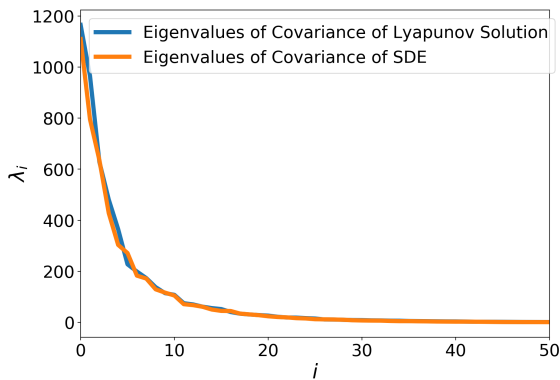


Figure 16: Eigenvalues of \mathbf{P}

4 Quantifying conditions for successful task learning

4.1 Introduction

With the intrinsic manifold found, we are now in a position to investigate the ability of the test subject to re-learn the correct movements when the mapping from neural activity to cursor velocity is changed. Sadtler et al. found that choosing the mapping \mathbf{C} within the intrinsic manifold resulted in successful task learning, while the subject failed to learn to generate movements under an outside-manifold perturbation. Similarly to how we defined the intrinsic manifold, the key metric under consideration is the amount of variance of the neural space accounted for, this time by

the choice of mapping, \mathbf{C} , so

$$V = \text{trace}(\mathbf{C}\Sigma\mathbf{C}^T) \quad (14)$$

It will be investigated how task performance depends on the amount of variance explained.

An initial set of mappings to be tested will be created by sliding 2-column wide window across the basis for the neural space (of which the first 21 columns define the intrinsic manifold), such that each set of neighbouring two columns defines one choice of mapping, \mathbf{C} . The columns are arranged in order of decreasing eigenvalue, so as the window is slid across the matrix, the eigenvalues decrease, so the variance accounted goes from maximum variance to minimum variance. Geometrically, as the window is slid across the matrix, the choice of BCI mapping aligns less and less well with the intrinsic manifold. Alternatively any two columns of the intrinsic manifold can be combined to give one \mathbf{S} . For 21 columns, this gives 210 unique data points, some of which will already have been accounted for in the set of \mathbf{S} s above. Finally, instead of just choosing columns from the basis \mathbf{S} or intrinsic manifold, one can generate random orthogonal columns. Let \mathbf{H} be a 2×200 matrix of random points samples from a normal distribution. Performing QR decomposition (SVD) on \mathbf{H} and taking \mathbf{S} as the Q -factor yields a random orthonormal mapping.

4.2 Steady State Solution

Consider the state-space system as defined in Equation 10. For a given desired steady state activity, we can solve this in steady state to find the constant input vector \mathbf{u} that leads to steady state convergence.

By definition, at steady state $\dot{\mathbf{x}} = 0$, so we can write:

$$0 = \mathbf{A}\mathbf{x} + \mathbf{B}\mathbf{u} + \bar{\mathbf{h}} \quad (15)$$

Rearranging:

$$\mathbf{x} = -\mathbf{A}^{-1}(\mathbf{B}\mathbf{u} + \bar{\mathbf{h}}) \quad (16)$$

Neural activity is mapped to cursor velocity as follows:

$$\mathbf{v} = \mathbf{C}\mathbf{x} \quad (17)$$

so substituting in for \mathbf{x} gives:

$$\mathbf{v} = -\mathbf{C}\mathbf{A}^{-1}(\mathbf{B}\mathbf{u} + \bar{\mathbf{h}}) \quad (18)$$

Denote the desired steady-state velocity by \mathbf{v}^* , and define the squared error as $\epsilon = \|\mathbf{v} - \mathbf{v}^*\|_2^2$. To find the value of \mathbf{u} that minimises the error, substitute in for \mathbf{v} :

$$\begin{aligned} \epsilon &= (-\mathbf{C}\mathbf{A}^{-1}(\mathbf{B}\mathbf{u} + \bar{\mathbf{h}}) - \mathbf{v}^*)^T \\ &\quad (-\mathbf{C}\mathbf{A}^{-1}(\mathbf{B}\mathbf{u} + \bar{\mathbf{h}}) - \mathbf{v}^*) \end{aligned} \quad (19)$$

by definition of the \mathcal{L}_2 norm. Expanding:

$$\begin{aligned} \epsilon &= (-\mathbf{C}\mathbf{A}^{-1}(\mathbf{B}\mathbf{u} + \bar{\mathbf{h}}))^T(-\mathbf{C}\mathbf{A}^{-1}(\mathbf{B}\mathbf{u} + \bar{\mathbf{h}})) \\ &\quad + \mathbf{v}^{*T}(\mathbf{C}\mathbf{A}^{-1}(\mathbf{B}\mathbf{u} + \bar{\mathbf{h}})) + \\ &\quad (\mathbf{C}\mathbf{A}^{-1}(\mathbf{B}\mathbf{u} + \bar{\mathbf{h}}))^T\mathbf{v}^* + \mathbf{v}^{*T}\mathbf{v}^* \end{aligned} \quad (20)$$

Let $\mathbf{M} \triangleq -\mathbf{C}\mathbf{A}^{-1}\mathbf{B}$ and $\mathbf{n} \triangleq -\mathbf{C}\mathbf{A}^{-1}\bar{\mathbf{h}}$.

Then:

$$\begin{aligned} \epsilon &= \mathbf{u}^T \mathbf{M}^T \mathbf{M} \mathbf{u} + \mathbf{n}^T \mathbf{M} \mathbf{u} + \mathbf{u}^T \mathbf{M}^T \mathbf{n} + \\ &\quad \mathbf{n}^T \mathbf{n} - \mathbf{v}^{*T} \mathbf{M} \mathbf{u} - \mathbf{u}^T \mathbf{M}^T \mathbf{v}^* - \mathbf{v}^{*T} \mathbf{n} - \\ &\quad \mathbf{n}^T \mathbf{v}^* + \mathbf{v}^{*T} \mathbf{v}^* \end{aligned} \quad (21)$$

Find the minimum by differentiating with respect to \mathbf{u} , set to 0 and solve for \mathbf{u}

$$\begin{aligned} \frac{d\epsilon^2}{d\mathbf{u}} &= 2\mathbf{M}^T \mathbf{M} \mathbf{u} + 2(\mathbf{n}^T \mathbf{M})^T \\ &\quad - 2\mathbf{M}^T \mathbf{v}^* = 0 \end{aligned} \quad (22)$$

Therefore

$$\mathbf{M}^T \mathbf{M} \mathbf{u} = \mathbf{M}^T(\mathbf{v}^* - \mathbf{n}) \quad (23)$$

This value of \mathbf{u} thus gives the minimum error and so is the best constant input possible for convergence towards a steady-state value. The condition number $\text{cond}(\mathbf{M}^T \mathbf{M}) \sim \mathcal{O}(10^{18})$, so the matrix $\mathbf{M}^T \mathbf{M}$ is non-invertible. This is expected, as \mathbf{M} is defined as $\mathbf{M} = -\mathbf{C}\mathbf{A}^{-1}\mathbf{B}$ and \mathbf{C} is low-rank. There will therefore not be a unique solution, however one solution can be found by pre-multiplying both sides by \mathbf{M} :

$$\mathbf{M}\mathbf{M}^T \mathbf{M} \mathbf{u} = \mathbf{M}\mathbf{M}^T(\mathbf{v}^* - \mathbf{n})$$

$\mathbf{M}\mathbf{M}^T$ is invertible, so:

$$\mathbf{M} \mathbf{u} = (\mathbf{M}\mathbf{M}^T)^{-1} \mathbf{M}\mathbf{M}^T(\mathbf{v}^* - \mathbf{n})$$

By inspection, we can see that the solution is:

$$\mathbf{u} = \mathbf{M}^T(\mathbf{M}\mathbf{M}^T)^{-1}(\mathbf{v}^* - \mathbf{n}) \quad (24)$$

This expression for \mathbf{u} can be simplified further by taking the SVD of \mathbf{M} . Let $\mathbf{M} = \mathbf{U}\mathbf{S}\mathbf{V}^T$,

then $\mathbf{M}\mathbf{M}^T = \mathbf{U}\mathbf{S}\mathbf{V}^T\mathbf{V}\mathbf{S}\mathbf{U}^T = \mathbf{U}\mathbf{S}^2\mathbf{U}$, as $\mathbf{V}^T\mathbf{V} = \mathbf{I}$ by definition. Substituting:

$$\mathbf{u} = \mathbf{V}\mathbf{S}\mathbf{U}^T(\mathbf{U}\mathbf{S}^{-2}\mathbf{U}^T)(\mathbf{v}^* - \mathbf{n})$$

This simplifies to:

$$\mathbf{u} = \mathbf{V}\mathbf{S}^{-1}\mathbf{U}^T(\mathbf{v}^* - \mathbf{n}) \quad (25)$$

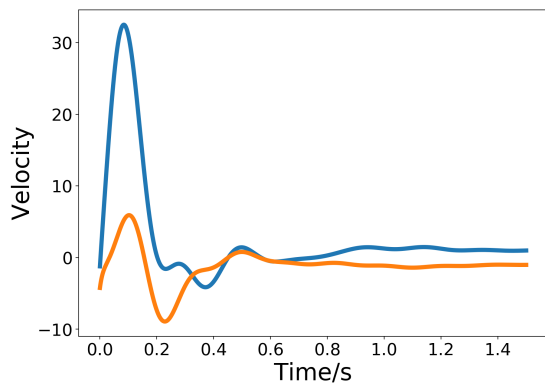


Figure 17: Output velocity during optimal constant input, as given by Equation 25.

Figure 17 shows the evolution of cursor velocity with time when the desired steady-state velocity is $\mathbf{v}^* = (1, -1)$ and the constant input \mathbf{u} is found using Equation 25. There is large initial transience, however after roughly 1 second the velocity has converged to $(1, -1)$.

Defining the required input energy to achieve the desired steady-state velocity as $\|\mathbf{u}\|_2^2$, we now have a measure of the performance. This can be calculated for each choice of mapping described in section 4.1. In the context of this model, the phenomenon observed by Sadler would manifest itself in an inverse relationship between the variance accounted for by

the mapping and the energy of the control-input, such that the more variance is explained by the mapping, the less energy is needed to control the system.

Figure 18 shows the energy of the steady-state solution for each of the test mappings described in the above section, plotted on a log-log plot. The black points are mappings formed from neighbouring columns of the matrix of all eigenvectors, \mathbf{S} . On a large scale, we see that sliding the window across the columns of the eigenvectors, decreasing the variance accounted for by the columns causes the energy of the steady-state solution to increase, which correlates with the monkeys not being able to learn the task. At the upper limit of variance explained, so the top columns of \mathbf{S} , the data points stop following the trend, instead even increasing a small amount. This is confirmed by the data points corresponding to all combinations of columns of the intrinsic manifold (red crosses). Rather than decreasing in energy, we see that the data points just form a cloud. It is not obvious why the trend breaks down here. The random mappings behave similarly. The cloud of points is centred on twice the mean variance explained (as the mapping consists of two vectors), however there is no relationship between the amount of variance explained and solution energy at such small ranges of variance. The colours representing the different choices of \mathbf{C} will be consistent across all future plots in this section.

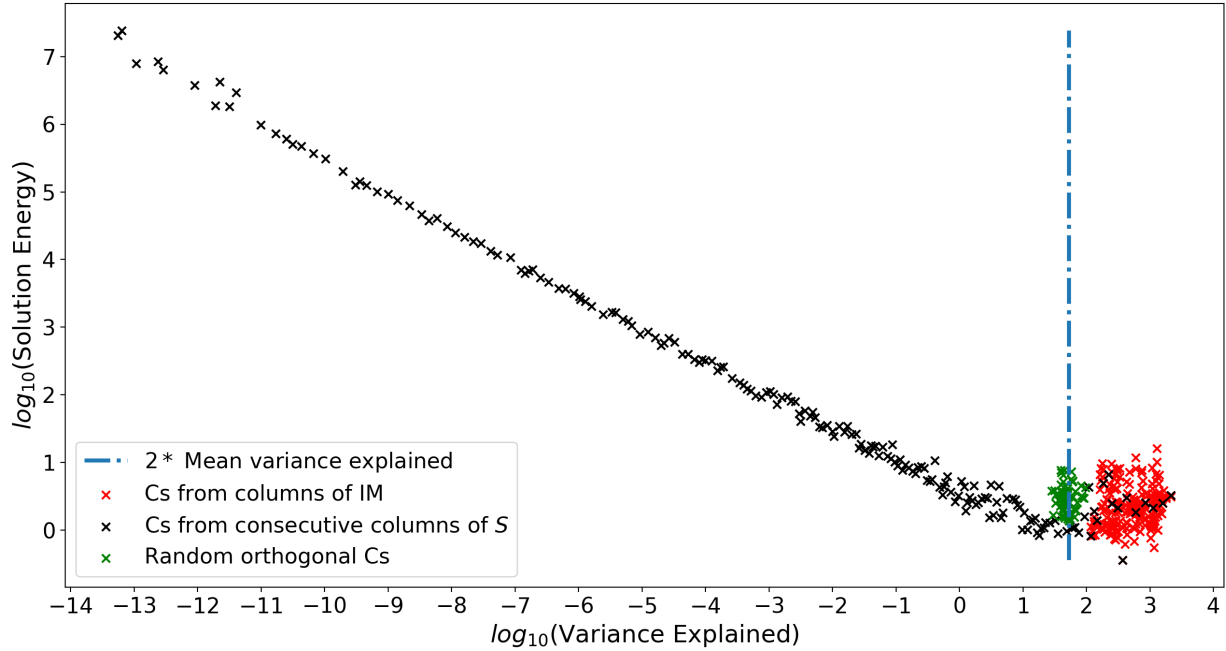


Figure 18: Solution Energy $\mathbf{u}^T \mathbf{u}$ plotted against the variance explained by the choice of mapping \mathbf{C} . Red: Combinations of columns from the intrinsic manifold. Black: Mappings consisting of 2 consecutive columns of \mathbf{S} . Green: Random orthonormal mappings

4.3 Optimal Tracking

While steady-state analysis has an analytic solution, it does not accurately simulate the way in which a monkey would reach for a target, as there is no feedback between the desired velocity and the current velocity. This results in the large transients seen in Figure 17. Ideally the test subject would achieve the desired velocity as quickly as possible with minimal deviation. The problem can instead be solved using methods of optimal control. This will ensure minimal deviation, removing the large transients seen in Figure 17. We can generalise the problem by requiring the output to track a random desired reference signal.

Rather than having a constant input, as in section 4.2, at each time step the controller should take the desired velocity at that time instant and the actual velocity and compute the optimal input.

4.3.1 Gaussian Processes

It was decided that the velocity profile to be tracked would be defined by a gaussian process. A gaussian process is an infinite-dimensional multivariate normal distribution, sampled at desired intervals. The covariance matrix chosen to define the distribution was generated by sampling from a squared exponential function. The dimensionality of the

output is two, thus we will create two independent gaussian processes for the control system to track.

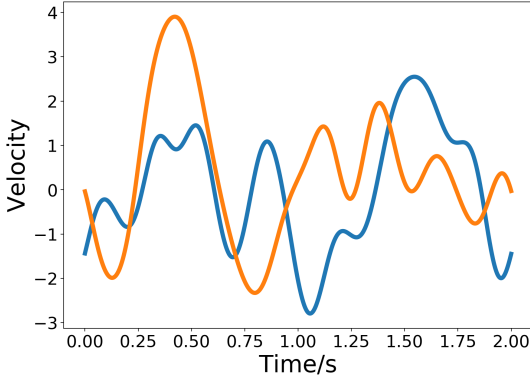


Figure 19: Two independent gaussian processes

Figure 19 shows the two gaussian processes generated to use as reference signals. An important parameter in their creation is the characteristic length-scale. A longer length-scale leads to a process that varies much more slowly. To most accurately simulate the dynamics of the brain, the length-scale was chosen to be the time constant of the differential equation defining the activity in the motor cortex, $\lambda = 0.15$.

4.3.2 Linear Quadratic Integral (LQI) Optimal Control

We now aim to design an optimal controller to track the two gaussian processes created

above. Consider the state space system

$$\begin{aligned}\dot{\mathbf{x}}_1 &= \mathbf{A}_1 \mathbf{x}_1 + \mathbf{B}_1 \mathbf{u} \\ \mathbf{y}_1 &= \mathbf{C}_1 \mathbf{x}_1\end{aligned}\quad (26)$$

It is desired to track reference signal \mathbf{v} . We define the tracking error as

$$\mathbf{e}_1 = \mathbf{v} - \mathbf{y}_1 = \mathbf{v} - \mathbf{C}_1 \mathbf{x}_1 \quad (27)$$

Integrating the error gives

$$\mathbf{x}_2 = \int_0^t \mathbf{e}_1(\tau) d\tau \quad (28)$$

This is appended to the system to give extended dynamics

$$\begin{aligned}\left(\begin{array}{c} \dot{\mathbf{x}}_1 \\ \dot{\mathbf{x}}_2 \end{array} \right) &= \left(\begin{array}{cc} \mathbf{A}_1 & \mathbf{0} \\ -\mathbf{C}_1 & \mathbf{0} \end{array} \right) \left(\begin{array}{c} \mathbf{x}_1 \\ \mathbf{x}_2 \end{array} \right) \\ &+ \left(\begin{array}{c} \mathbf{B}_1 \\ \mathbf{0} \end{array} \right) \mathbf{u} + \left(\begin{array}{c} \mathbf{0} \\ \mathbf{I} \end{array} \right) \mathbf{v}\end{aligned}\quad (29)$$

We can now write this as

$$\dot{\mathbf{x}} = \mathbf{Ax} + \mathbf{Bu} + \mathbf{Gv} \quad (30)$$

The new error for the system in Equation 30 is

$$\mathbf{e} = \left(\begin{array}{c} \mathbf{v} - \mathbf{C}_1 \mathbf{x}_1 \\ \mathbf{x}_2 \end{array} \right) = \mathbf{Mv} + \overline{\mathbf{C}}\mathbf{x} \quad (31)$$

with

$$\mathbf{M} = \left(\begin{array}{c} \mathbf{I} \\ \mathbf{0} \end{array} \right), \quad \overline{\mathbf{C}} = \left(\begin{array}{cc} -\mathbf{C}_1 & \mathbf{0} \\ \mathbf{0} & \mathbf{I} \end{array} \right)$$

We wish to find an optimal controller to minimise the cost function

$$J = \int_0^\infty (\mathbf{e}^T \mathbf{Q} \mathbf{e} + \mathbf{u}^T \mathbf{R} \mathbf{u}) dt, \quad (32)$$

subject to Equation 30, where $\mathbf{Q} = \mathbf{Q}^T$ is positive semi-definite and $\mathbf{R} = \mathbf{R}^T$ is positive definite. Substituting gives

$$J = \int_0^\infty (\mathbf{x}^T \bar{\mathbf{C}}^T \mathbf{Q} \bar{\mathbf{C}} \mathbf{x} + 2\mathbf{v}^T \mathbf{M}^T \mathbf{Q} \bar{\mathbf{C}} \mathbf{x} + \mathbf{v}^T \mathbf{M}^T \mathbf{Q} \mathbf{M} \mathbf{v} + \mathbf{u}^T \mathbf{R} \mathbf{u}) dt \quad (33)$$

Standard methodology, as outlined in Bryson, leads to the following Riccati equation

$$\dot{\mathbf{P}} = -\mathbf{P}\mathbf{A} - \mathbf{A}^T\mathbf{P} - \bar{\mathbf{C}}^T \bar{\mathbf{C}} + \mathbf{P}\mathbf{B}\mathbf{R}^{-1}\mathbf{B}^T\mathbf{P} \quad (34)$$

Assuming that (\mathbf{A}, \mathbf{B}) is controllable and (\mathbf{A}, \mathbf{C}) is observable, there exists a unique solution to the Riccati Equation, Equation 34, at steady state ($\dot{\mathbf{P}} = 0$), \mathbf{P}_{ss} . The control law can then be written as

$$\mathbf{u} = -\mathbf{K}_x \mathbf{x} - \mathbf{K}_v \mathbf{v} \quad (35)$$

where

$$\begin{aligned} \mathbf{K}_x &= \mathbf{R}^{-1} \mathbf{B}^T \mathbf{P}_{ss} \\ \mathbf{K}_v &= \mathbf{R}^{-1} \mathbf{B}^T (\mathbf{P}_{ss} \mathbf{B} \mathbf{R}^{-1} \mathbf{B}^T - \mathbf{A}^T)^{-1} \\ &\quad (\bar{\mathbf{C}}^T \mathbf{Q} \mathbf{M} + \mathbf{P}_{ss} \mathbf{G}) \end{aligned}$$

The closed-loop system can therefore be written as

$$\begin{aligned} \dot{\mathbf{x}} &= (\mathbf{A} - \mathbf{B}\mathbf{K}_x)\mathbf{x} + (\mathbf{G} - \mathbf{B}\mathbf{K}_v)\mathbf{v} \\ &= \bar{\mathbf{A}}\mathbf{x} + \bar{\mathbf{B}}\mathbf{v} \end{aligned} \quad (36)$$

We can now implement this controller to track the gaussian processes created in Section 4.3.1. We would also like to investigate how the controller performs under a step reference input. In Figure 20, the reference signals are

shown in blue and orange, with the output of the closed-loop system in green and red. The controller manages to track the step and the gaussian processes. There is larger deviation in the green trace than the red for both the step and gaussian process tracking.

It is to be noted that the \mathbf{Q} and \mathbf{R} cost function matrices were set to simply be identity; to achieve better tracking performance one could for example, multiply \mathbf{R} by some constant $\lambda < 1$, which would penalise the inputs less. Larger energy inputs would then be allowed, leading to better tracking, as is shown in Figure 21. In this case, however, the absolute performance of the tracking is less important than the relative performance when varying the choice of mapping \mathbf{C}_1 .

4.3.3 Numerical measurement of error

The augmentation of the system means that it is not possible to calculate a measure of performance analytically, however one can measure the error numerically. There are two options regarding the tracking error. The first is to measure the instantaneous tracking error vector \mathbf{e}_1 at each time point, find the squared norm and sum across each time step. The second option is to use the error total error vector \mathbf{e} as defined by the augmented system. This is length 4 vector at each time point, the first two components being \mathbf{e}_1 and the second being the integral of \mathbf{e}_1 up until the current

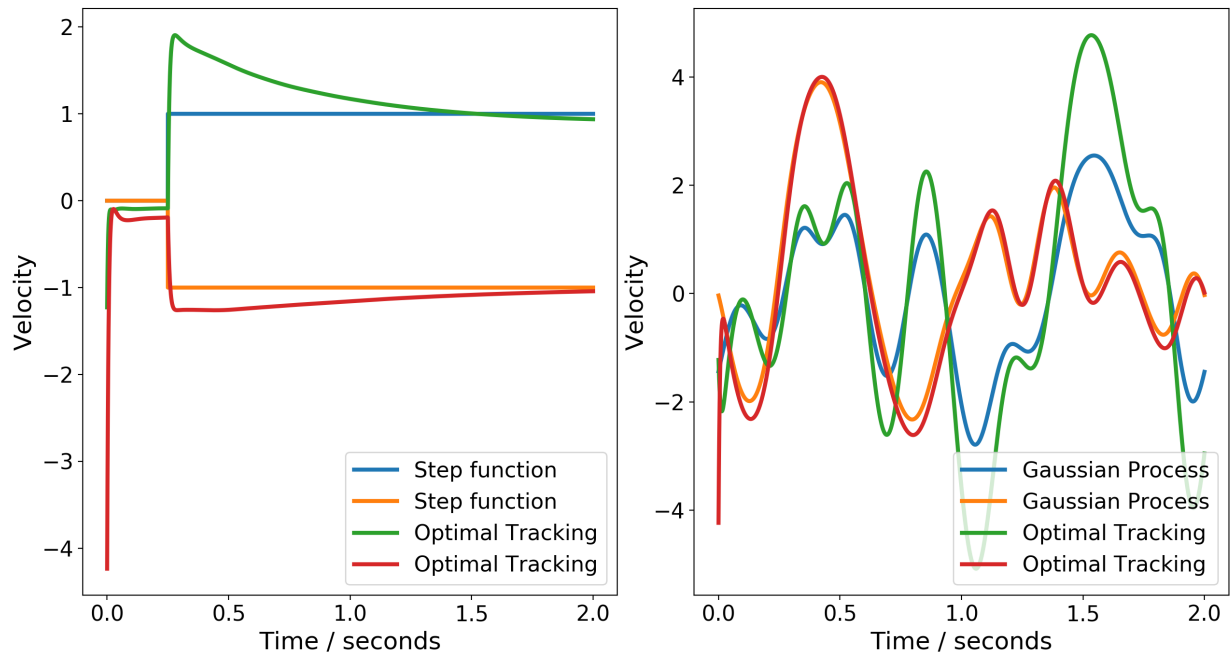


Figure 20: Left: Step response, Right: Gaussian process tracking. $\lambda_R = 1$

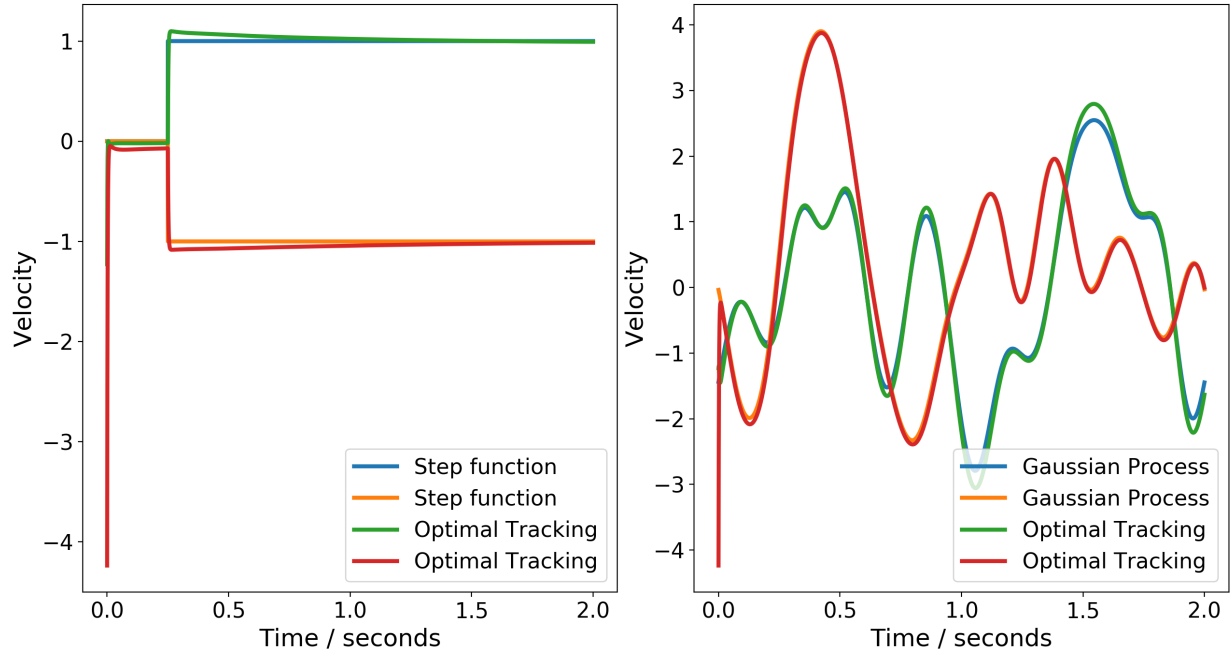


Figure 21: Left: Step response, Right: Gaussian process tracking. $\lambda_R = 0.1$

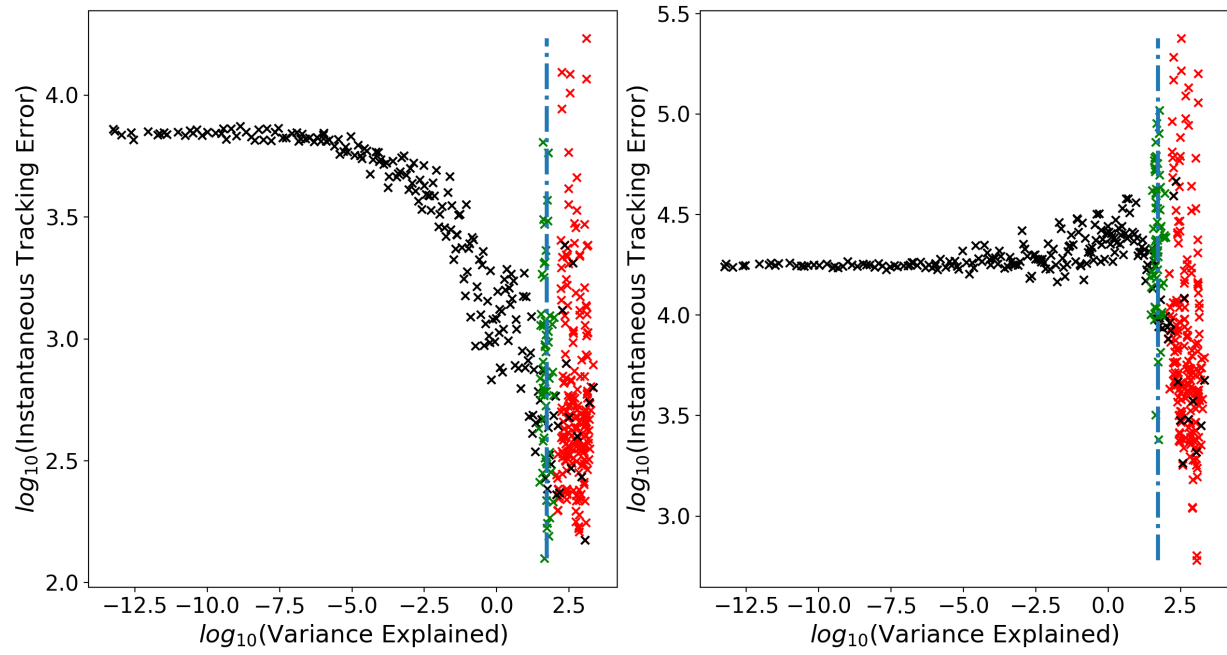


Figure 22: Integral of the instantaneous tracking error under optimal LQI control, $\int e_1^T e_1 dt$
 Left: Step input tracking. Right: Gaussian process tracking

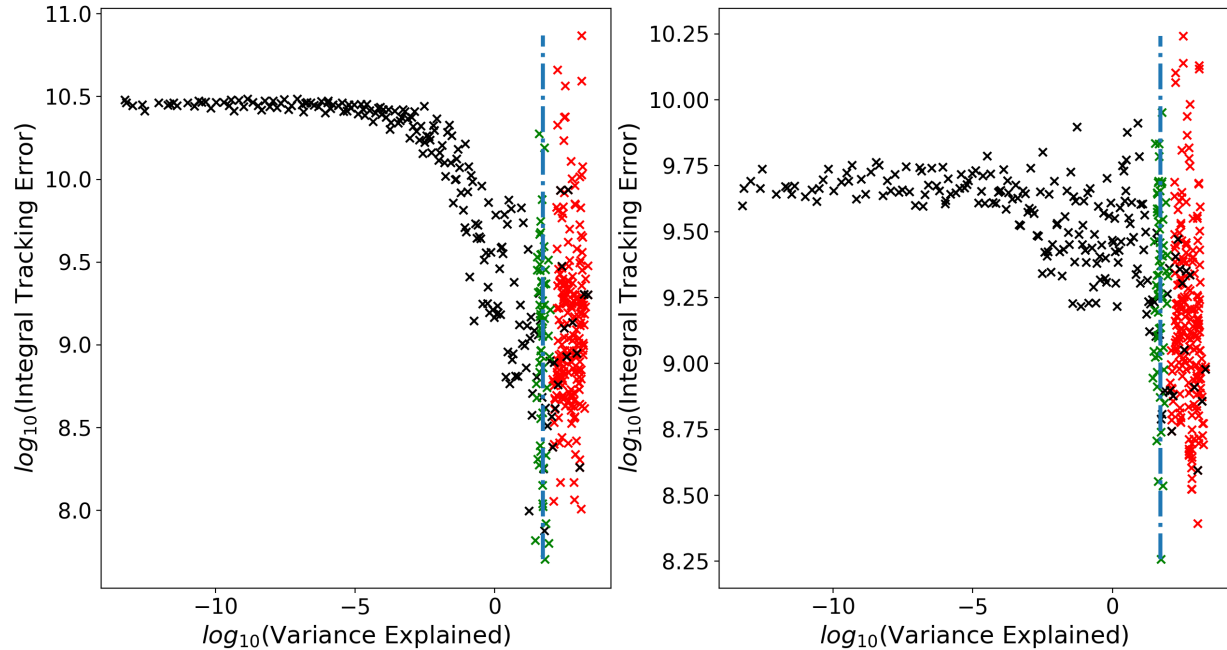


Figure 23: Integral of the augmented tracking error under optimal LQI control, $\int e^T e dt$
 Left: Step input tracking. Right: Gaussian process tracking

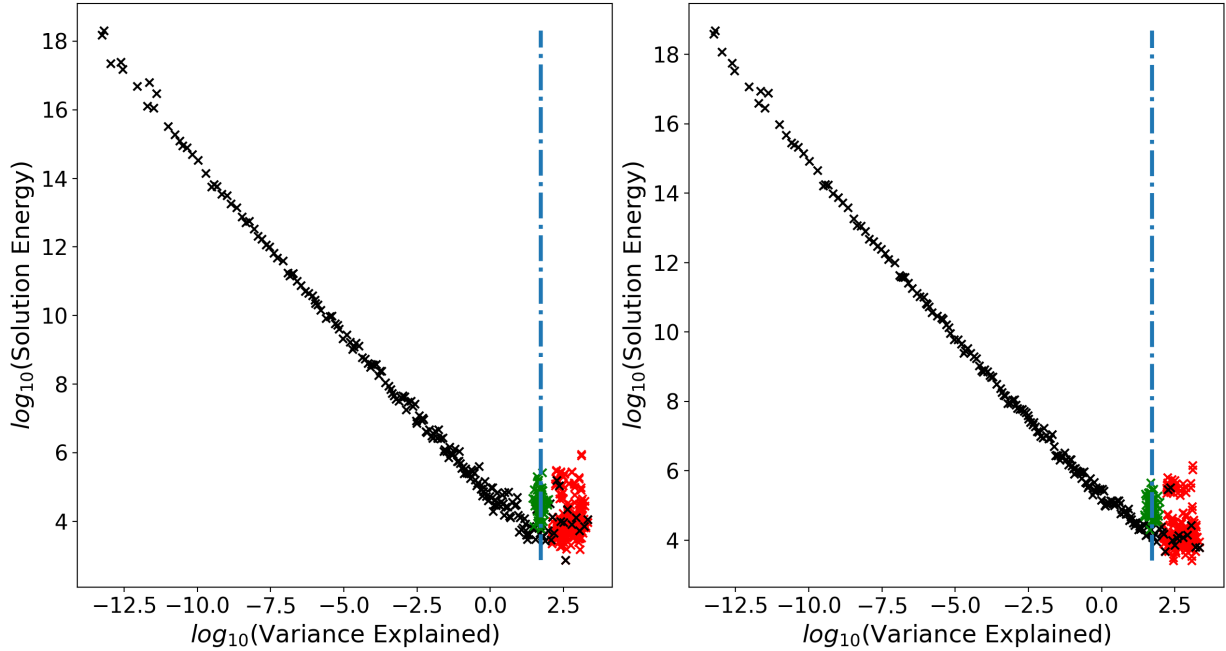


Figure 24: Control-input energy, $\int \mathbf{u}^T \mathbf{u} dt$ Left: Step input tracking. Right: Gaussian process tracking

time point. Figures 22, 23 and 24 show the relationship between both definitions of tracking error and the control input energy and the variance explained by the chosen mapping for both the step input tracking and the gaussian process tracking.

4.4 State LQR

While the LQI optimal tracking performed well, it was only possible to measure the error numerically. An alternative method of simulating the task performed by the monkey is to perform state LQR. Rather than defining a generic random process to track, this more closely models the experiment, by defining

a desired steady-state target velocity. The pseudo-inverse of \mathbf{C} is used to find one of many vectors \mathbf{x} that would give the desired output and then LQR is applied to reach that state optimally. This method is more similar to the constant input steady-state solution described in Section 4.2, however the application of LQR means that the large transients observed under constant control input will not be seen. Using state LQR has the advantage that the cost function can be found analytically, as opposed to the numerical method used above.

Consider the state space system in Equation 26. Define

$$\mathbf{x}^* = \mathbf{C}^\dagger \mathbf{y} \quad (37)$$

where as before C^\dagger is the pseudo-inverse of $\mathbf{B}^T \mathbf{B}$. Symmetry means that attempting to take the velocity from 0 to some steady-state value is identical to starting at that steady state value and letting the system take it to 0. We thus have the following system:

$$\dot{\mathbf{x}} = \mathbf{A}\mathbf{x} + \mathbf{B}\mathbf{u} \quad \mathbf{x}(0) = \mathbf{x}^* \quad (38)$$

The LQR cost function is then

$$J(\mathbf{x}(0), \mathbf{u}(\cdot)) = \int_0^\infty \mathbf{x}^T \mathbf{Q} \mathbf{x} + \mathbf{u}^T \mathbf{R} \mathbf{u} dt \quad (39)$$

The optimal control input is:

$$\mathbf{u} = -\mathbf{R}^{-1} \mathbf{B}^T \mathbf{X} \mathbf{x} \quad (40)$$

where \mathbf{X} is the solution to the control algebraic Riccati Equation

$$\mathbf{0} = \mathbf{I} + \mathbf{X}\mathbf{A} + \mathbf{A}^T \mathbf{X} - \mathbf{X}\mathbf{B}\mathbf{R}^{-1} \mathbf{B}^T \mathbf{X} \quad (41)$$

The optimal cost J is given by

$$J = \mathbf{x}^{*T} \mathbf{X} \mathbf{x}^* \quad (42)$$

This cost consists of the state cost $\mathbf{x}^T \mathbf{Q} \mathbf{x}$ and the control input energy $\mathbf{u}^T \mathbf{R} \mathbf{u}$. We can analytically calculate their individual values as follow: Consider the closed loop system with optimal control inputs

$$\dot{\mathbf{x}} = (\mathbf{A} - \mathbf{B}\mathbf{R}^{-1} \mathbf{B}^T \mathbf{X})\mathbf{x} = (\mathbf{A} - \mathbf{B}\mathbf{K})\mathbf{x} \quad (43)$$

This has solution

$$\mathbf{x} = \mathbf{x}^* e^{t(\mathbf{A} + \mathbf{B}\mathbf{K})} \quad (44)$$

and so

$$\mathbf{u} = \mathbf{K}\mathbf{x}^* e^{t(\mathbf{A} + \mathbf{B}\mathbf{K})} \quad (45)$$

Therefore

$$\begin{aligned} \int_0^\infty \mathbf{u}^T \mathbf{u} dt &= \\ \mathbf{x}^{*T} \int_0^\infty e^{t(\mathbf{A} + \mathbf{B}\mathbf{K})} \mathbf{K}^T \mathbf{K} e^{t(\mathbf{A} + \mathbf{B}\mathbf{K})} dt \mathbf{x}^* & \end{aligned} \quad (46)$$

Denoting the integral as Q , Q is the solution to the Lyapunov Equation

$$(\mathbf{A} + \mathbf{B}\mathbf{K})^T \mathbf{Q} + \mathbf{Q}(\mathbf{A} + \mathbf{B}\mathbf{K}) + \mathbf{K}^T \mathbf{K} = 0 \quad (47)$$

Thus

$$\int_0^\infty \mathbf{u}^T \mathbf{u} dt = \mathbf{x}^{*T} \mathbf{Q} \mathbf{x}^* \quad (48)$$

It follows that

$$\int_0^\infty \mathbf{x}^T \mathbf{x} dt = J - \int_0^\infty \mathbf{u}^T \mathbf{u} dt \quad (49)$$

$$= \mathbf{x}^{*T} \mathbf{X} \mathbf{x}^{*T} - \mathbf{x}^{*T} \mathbf{Q} \mathbf{x}^* \quad (50)$$

4.4.1 Performance Measures

Figure 25 shows the state cost, $\int_0^\infty \mathbf{x}^T \mathbf{x} dt$ and control energy, $\int_0^\infty \mathbf{u}^T \mathbf{u} dt$, calculated as described above. In contrast to the results obtained using steady-state methods or LQI, the control energy does not display a strong inverse relationship. Instead it has very little structure to it, even showing some significant increases as the variance explained increases, before decreasing again. The state cost, however, shows a similar pattern to that observed during LQI control. As the variance decreases, the cost increases steeply, before flattening out. It is notable that this is the first time that the red points generated from the combinations of columns of the intrinsic manifold appear to be following the trend. Previously,

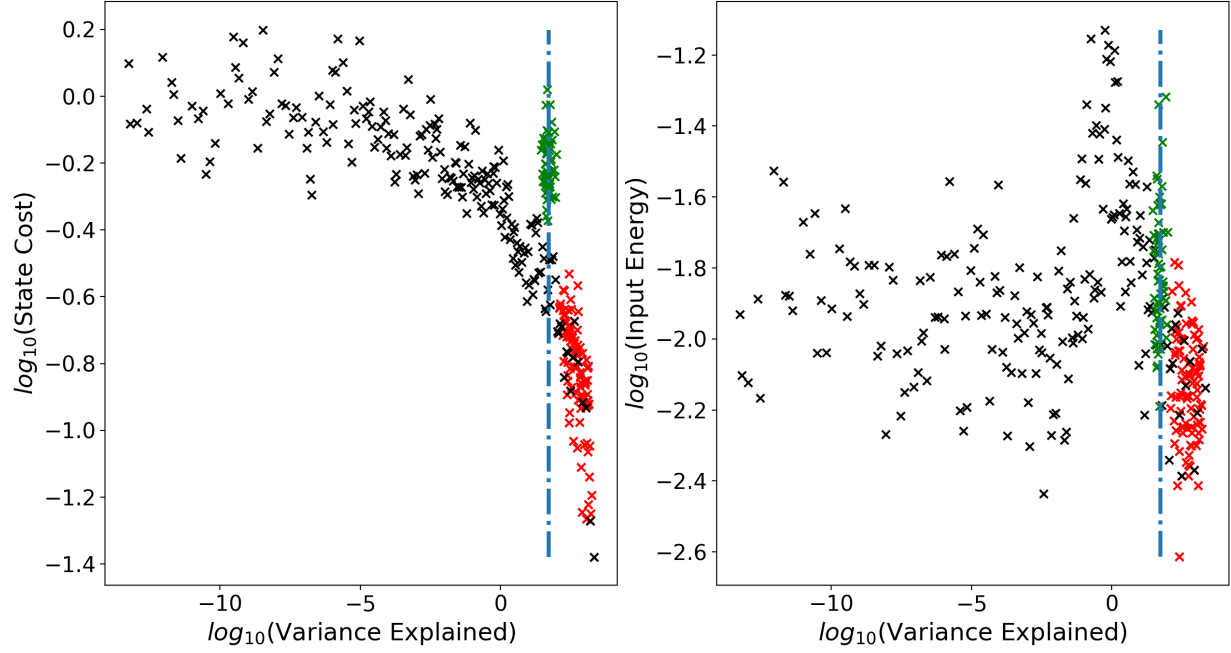


Figure 25: Left: LQR State Cost. Right: LQR Control Energy. Black: Consecutive columns of S . Red: Combinations of columns of the intrinsic manifold. Green: Random orthonormal mappings.

they formed clouds of points that had to relate to the rest of the data (eg Figure 22 or Figure 24). The gradient of the curve at the upper limit of variance and the amount of noise in the data means we cannot be sure that this is not just another cloud, however it does appear to be an improvement on previous methods. On the other hand, the points generated from random mappings do not lie on the curve at all, having a much larger state cost compared to other points of similar variance. This is consistent with their behaviour previously.

4.4.2 Bisection

A problem with using either of these as a measure of performance is that they are dependent on each other. Higher energy inputs allowed would result in better tracking, so lower tracking error. This means that data-points aren't directly comparable. The overall cost J may be optimal, but it is not known how that cost is split between the tracking error and the input energy. To overcome this problem, the matrices Q and R in the LQR cost function can be used. Previously, these had been set to identity. Multiplying either of these by a constant penalises the effect that either the state cost or the input energy has

on the total cost. The aim is to choose either Q or R (while the other remains identity) such that either the state cost or the input energy is constant across all choices of mapping, and so the other variable of interest can be meaningfully compared. In this case, we will fix the input energy to 10^{-2} , as the majority of the energies are close, so the bisection will be quicker. We thus define a constant λ_R to scale R . Increasing λ_R penalises the magnitude of the control-input energy. We would expect a larger λ_R to result in lower energies, however at the expense of a greater state cost. This is shown in Figure 26.

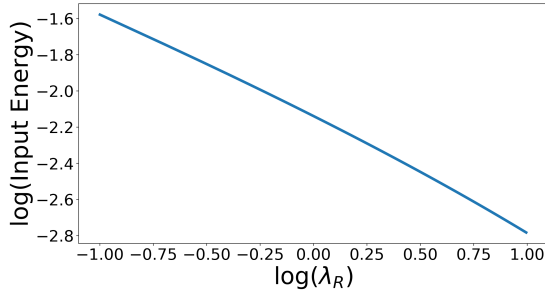


Figure 26: Evolution of LQR control-input energy as λ_R is increased. This is for one particular choice of mapping, C

Figure 27 shows the state costs with the input energy fixed to 0.01. There is minimal difference compared with Figure 25. A lot of the points in Figure 25 are close to the target input energy, so the change in state cost will be very small. The points showing the most change are the points created using mappings from the intrinsic manifold. We see that

they continue the trend of the black points, although there is still significant variability.

4.5 Discussion

We have seen that for all of the methods of control chosen, overall the measure of performance, whether that be control input energy or the state cost, decreases with an increasing amount of variance explained by the choice of control space. The steady-state method gave a very clean relationship, however the lack of feedback means that this is not a very good model for the monkey. Tracking a reference signal using linear quadratic integral control was a much better representation of how the monkey is performing a task. This gave a similarly clean relationship to the steady state method, however it is still not clear why this breaks down at the upper limit of the amount of variance explained. The magnitude of control-input energy for some the mappings with the most variance explained is larger than amount of energy needed to control mappings accounting for three to four orders of magnitude less variance. Using state LQR does not provide as clear a relationship as LQI control. This might be because the pseudo-inverse of the mapping was used to determine the required state. The mapping is low rank, so there are many choices of state that would lead to the correct output. By fixing one choice of state as the desired target state, we are removing the ability of the con-

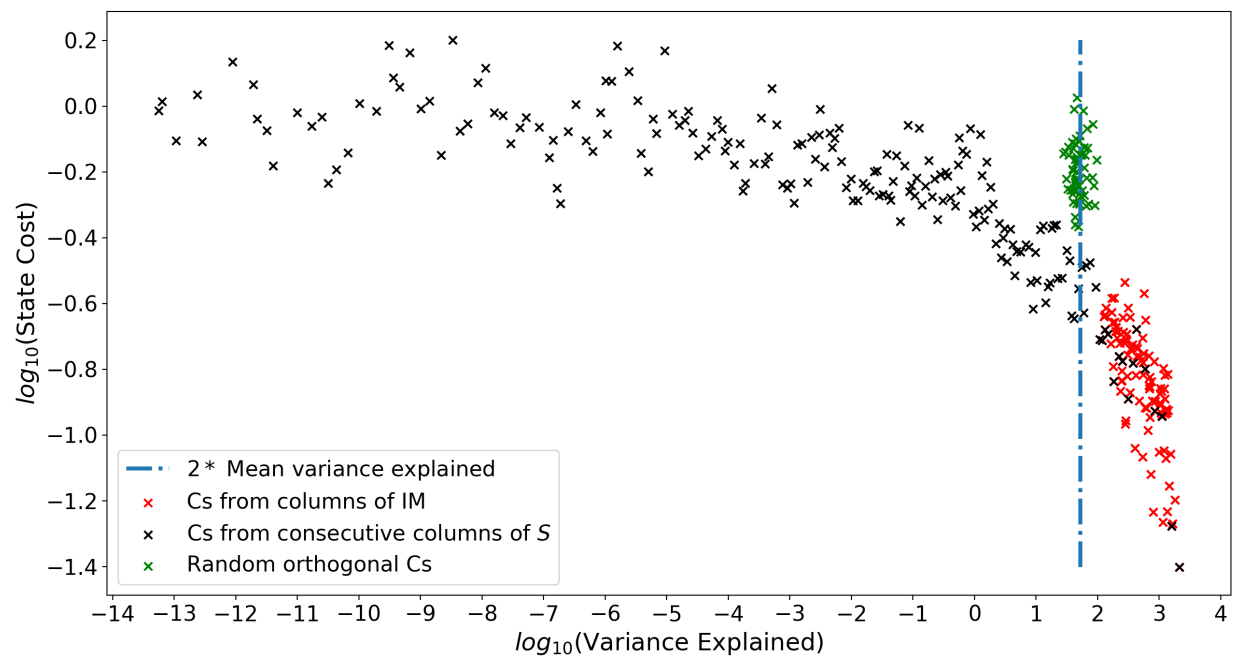


Figure 27: Left: LQR State Cost. Right: LQR Control Energy. Black: Consecutive columns of S . Red: Combinations of columns of the intrinsic manifold. Green: Random orthonormal mappings. Blue: Summing increasing numbers of columns of the intrinsic manifold. Bisection performed on the control input energy

trol system to lower the cost by finding other states that might have the same output but require less energy. Overall, however, it has been shown that the observation by Sadtler that task learnability depends on the properties of the BCI control space arises from the properties of the state-space system. We note that the solution to the Lyapunov equation (12), used to find the covariance of the system driven by noise, is, by definition, the controllability gramian \mathbf{P} . We see, therefore, that if the control space is aligned with the more controllable directions of \mathbf{P} , then the system will require less energy to control. This manifests itself in the monkey being able to learn the task more successfully.

4.6 Summary

It has been shown that there is a strong relationship between the amount of variance explained by the mapping and the ease of control, whether this be the state cost or the input energy. This agrees with the observations made by Sadtler et al. The directions that explain the largest amount of variance are those in the intrinsic manifold, so using a mapping that lies outside the intrinsic manifold will lead to poorer performance on the task.

5 Fixed Distribution Hypothesis

5.1 Introduction

As described in Section 2.2, Hennig et al. investigated whether there were any constraints on the activity in the null-space of the BCI. They found that the model that most closely fit the data was the Fixed Distribution Hypothesis, which propose that the distribution of null-space activity does not vary freely; instead it is constrained by the output-potent activity required to perform the task accurately. In this section, the Fixed Distribution Hypothesis will be modelled using the BCI simulation, to attempt to link the empirical observations made by Hennig et al. to the network model of M1. For each output-potent activity vector, the conditional distribution of output-null activity can be calculated and compared to the true samples. This will be compared to two other methods of generating the null-space activity. The first involves breaking the dependency of the null samples on the output potent activity, while the second is inspired by principles of minimum energy observed in muscular redundancy. If the BCI model is an accurate representation of the experimental task performed, the accuracy of the Fixed Distribution Hypothesis should be reflected in the data.

5.2 Tracking a long Gaussian Process

To collect a large sample of the activity with the maximum amount of variance possible, the optimal tracking paradigm of section 4.3 was used to track a 30-minute long gaussian process. This caused some problems, as the generating the squared exponential covariance matrix that defines the GP has computational complexity $\mathcal{O}(n^2)$, and so generating a 30-minute long gaussian process is not feasible. This was solved by instead forming the GP in Fourier space. First, a random Gaussian vector of the desired length was formed. The Fourier transform of the vector was then taken, and then each element i multiplied by $\exp((-\omega_i * l)^2/2)$, where l is the desired length-scale, and ω_i is the angular frequency component corresponding to the i -th element of the Fourier transform of the random vector. The inverse Fourier transform was then taken, giving a gaussian process of the desired length and length-scale. This algorithm has complexity $\mathcal{O}(n)$ rather than $\mathcal{O}(n^2)$, so can be implemented to generate long gaussian processes.

A similar problem arose when attempting to track this long gaussian process. This was more easily solved by splitting the process into shorter sections, tracking them individually, and then joining them back together to give the whole process. Hennig et al. only used a

within-manifold mapping to investigate the distribution of null-space activity, so the mapping C used in the tracking was defined to be the first two columns of the intrinsic manifold. We now have all of the data required to test the hypothesis.

5.3 Mapping to output-potent and output-null space

The samples collected must first be aligned with the control space such that the first two components of the activity correspond to the output-potent activity while the following 198 component correspond to output-null activity.. This was done by first finding the orthogonal complement of the mapping C . C has shape $(2, 200)$, so its complement has shape $(198, 200)$. These are then stacked together to form Q , which has shape $(200, 200)$. The transformed data y is then formed by $y = Qx$. The first two rows of y are now aligned with the output-potent directions of C , while the subsequent 198 rows are aligned with the output-null directions of C .

5.4 Modelling null-space activity

We will now model different ways of generating null-space activity and compare them with the null-space activity observed during tracking.

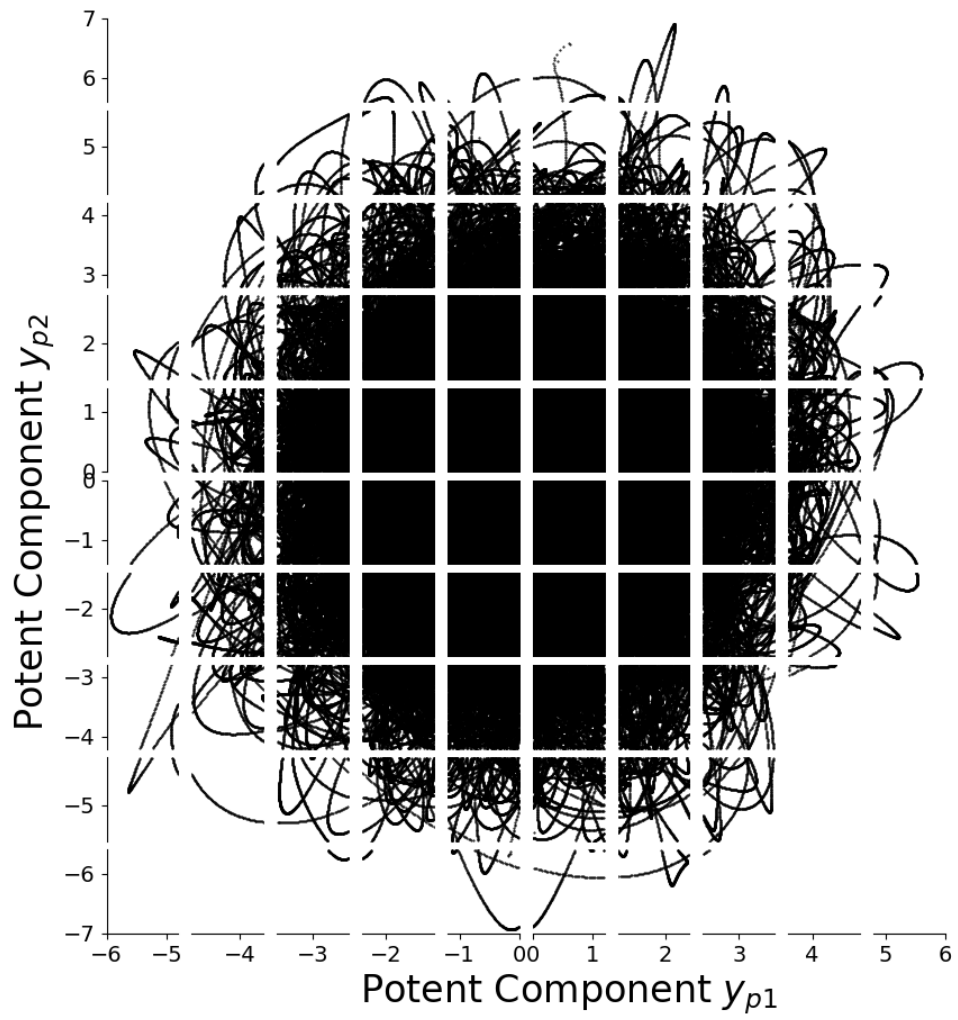


Figure 28: Output-potent components of y

5.4.1 Fixed Distribution Hypothesis

The fixed distribution hypothesis states that the underlying distribution of neural activity, and the distribution null-space activity for any given mapping is determined by the required potent activity. We thus calculate the conditional distribution of output-null activity for any given output-potent activity. To do this, the output-potent activity is sectioned into a 10-by-10 grid as shown in Figure 28. Now, for each of the 100 quadrants, the 198 null components corresponding to each data-point of potent activity that falls within the quadrant were also assigned to that quadrant. This enables us to investigate the distribution of null-space activity for that particular choice of output-potent activity. For each quadrant, we expect to see an individual distribution with some mean and variance.

The distribution of true null-samples in each quadrant can then be compared to the theoretical mean and variance of a conditional multivariate Gaussian. For a distribution $\mathbf{y} \sim \mathcal{N}(\boldsymbol{\mu}, \Sigma)$, with

$$\mathbf{y} = \begin{pmatrix} \mathbf{y}_p \\ \mathbf{y}_n \end{pmatrix}, \boldsymbol{\mu} = \begin{pmatrix} \boldsymbol{\mu}_p \\ \boldsymbol{\mu}_n \end{pmatrix}$$

$$\Sigma = \begin{pmatrix} \Sigma_{pp} & \Sigma_{np} \\ \Sigma_{pn} & \Sigma_{nn} \end{pmatrix}$$

where \mathbf{y}_p is the vector of 2 potent components and \mathbf{y}_n is the vector of 198 null components. The conditional distribution of \mathbf{y}_n

given \mathbf{y}_p is

$$p(\mathbf{y}_n | \mathbf{y}_p) = \mathcal{N}_n(\hat{\boldsymbol{\mu}}_n, \hat{\Sigma}_n) \quad (51)$$

with

$$\hat{\boldsymbol{\mu}}_n = \boldsymbol{\mu}_n + \Sigma_{pn}^T \Sigma_n^{-1} (\mathbf{y}_p - \boldsymbol{\mu}_p) \quad (52)$$

$$\hat{\Sigma}_n = \Sigma_{nn} - \Sigma_{pn}^T \Sigma_{pp}^{-1} \Sigma_{pn} \quad (53)$$

Figure 29 shows one example quadrant, with the true samples in blue plotted over samples from a normal distribution with mean and variance as defined in Equations 52 and 53 in black. Also shown is a contour depicting two standard deviations from the mean. For a gaussian distribution, this should capture 95% of the data.

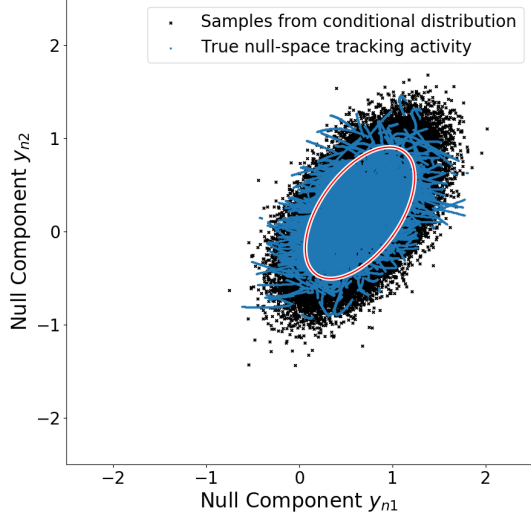


Figure 29: Black: Samples drawn from a conditional distribution defined by the mean and covariance matrix calculated in Equations 52 and 53. Blue: True samples from tracking activity. This plot shows the top two null components plotted against each other.

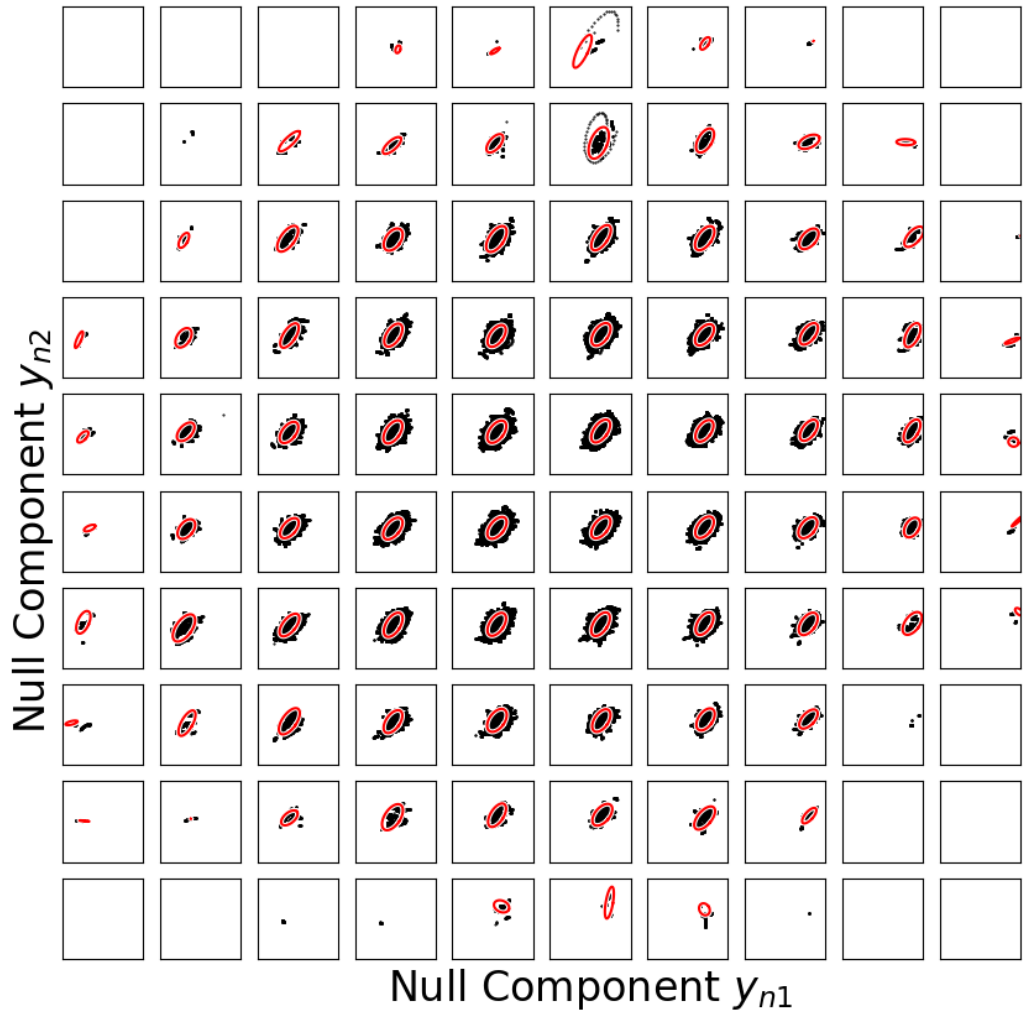


Figure 30: True null-space activity compared with the 2σ contour of the conditional distribution for the top two null components

We see that there is strong agreement between the true samples and the calculated conditional distribution. The mean and variance appear to be similar and the correlation between the two null components also agrees well. Figure 30 shows this result for all 100 quadrants. We see that the mean, variance and correlation varies across the quadrants. The fit is better for the quadrants with larger number of data points - the edge effects of the potent distribution (Figure 28) mean that the calculated conditional distribution will less accurately match the samples. Despite this, even at the edges we see that the size of the variance agrees well with the spread of the data. Figures 29 and 30 only show the conditional distribution for the top two components of \mathbf{y}_n , however any two null-space components can be plotted in this way. Repeats of Figure 30 using different components of \mathbf{y}_n can be found in Appendix B.

5.4.2 Breaking the dependence of null samples on potent activity

It has been shown that plotting the null components for given output potent components shows strong agreement with the theoretical conditional distribution. As a control, it is possible to break the dependency between the potent activity and its corresponding null activity. The simplest way to do this is to split the null components from the potent components, then shuffle them, so that there is no

longer any relationship between the potent and null, although it is important to maintain the marginal distribution of the null components for each data point. The shuffled null components are then rejoined to the potent components, and then assigned to their respective quadrants as previously. Figure 31 shows the same quadrant as Figure 29 having shuffled the null-space activity.

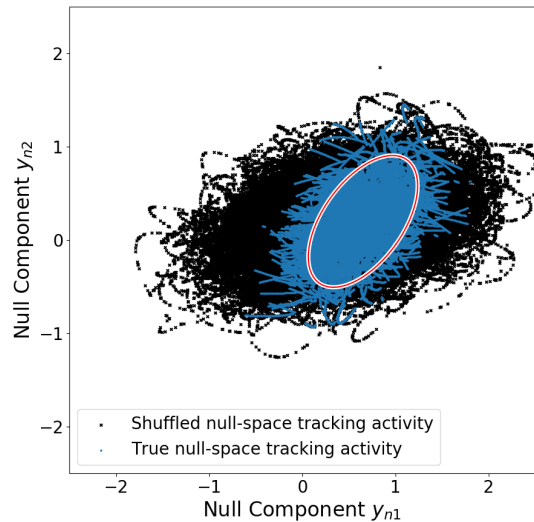


Figure 31: Top two components of null activity, with all null components shuffled before assigning to quadrants

The mean is incorrect, the variance of the shuffled samples is significantly greater than that of the true samples and the correlation is completely different. As before, this is repeated for all 100 quadrants, shown in Figure 32. The features observed on Figure 31 are consistent across all of the quadrants. Around the edges, the mean of the samples is much

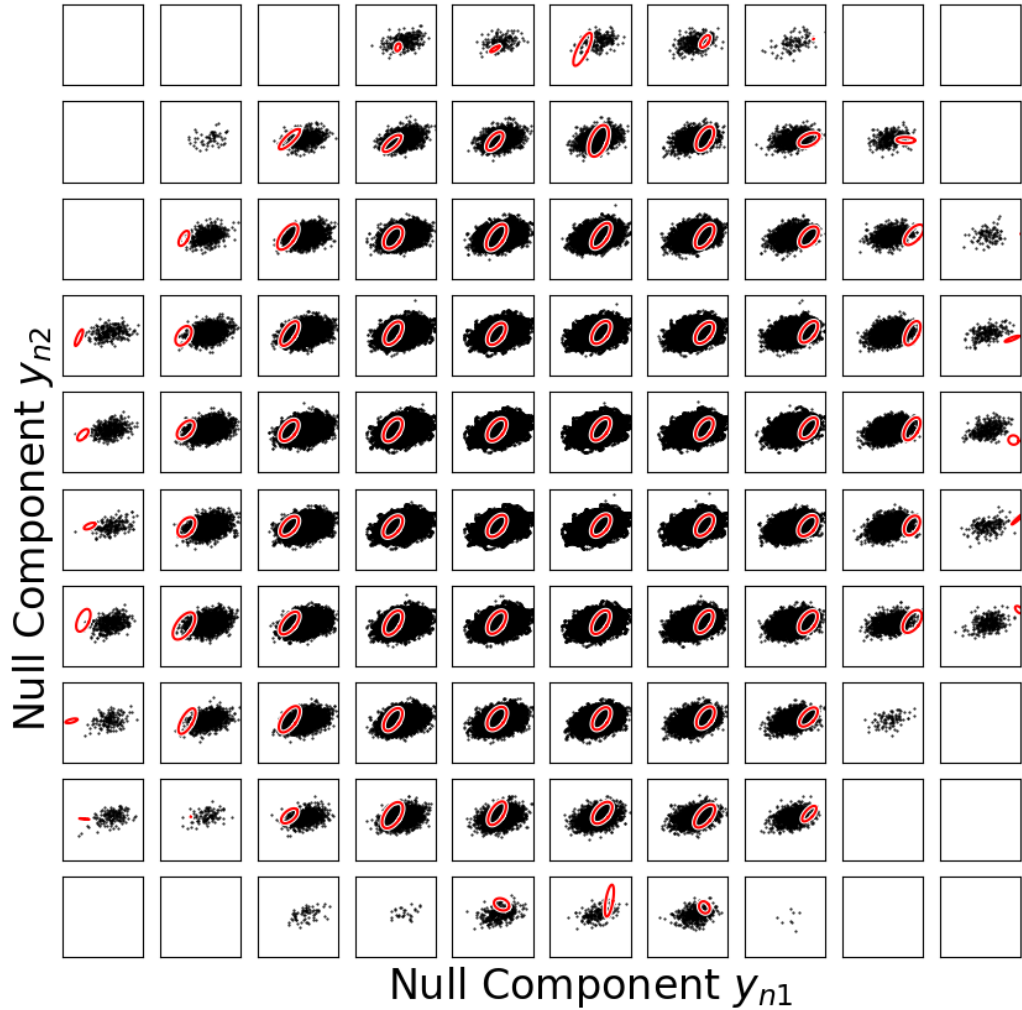


Figure 32: Distribution of shuffled null-space activity, top two components.

more significantly different than the example above, and the variances and correlations are consistently different to those of the actual null components. While it is clear from qualitative observations that shuffling the null activity causes the model to break down, a quantitative measure of fit would allow better comparison between the initial conditional samples and the shuffled data.

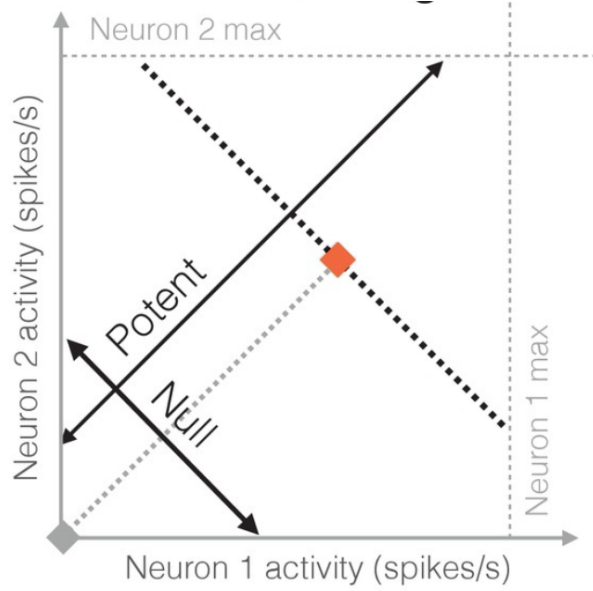


Figure 33: The dashed line shows all redundant activity patterns for the desired output-potent activity. The activity pattern with the lowest energy (orange square) is selected. (2)

5.4.3 Minimal Firing Hypothesis

One of the alternative hypotheses considered by Hennig et al. was the minimal firing hypothesis. This was inspired by studies of muscular redundancy, where it has been found that subjects use muscles so as to minimise total energy use. Analogously, as firing neurons costs energy, it may be that for all redundant firing patterns, the one that has the lowest total firing rate, and so the lowest energy, is selected. An example of this is shown in Figure 33.

The vector of null-activity for a given output potent activity was found through quadratic programming:

$$\min_x \quad \mathbf{x}^T \mathbf{x} \quad (54)$$

$$\text{subject to} \quad \overline{\mathbf{Q}}^T \mathbf{x} = \mathbf{y}_p \quad (55)$$

where $\overline{\mathbf{Q}}$ is the first two columns of \mathbf{Q} , such that $\overline{\mathbf{Q}}^T \mathbf{x}$ is a vector of size 2 and \mathbf{y}_p is the potent activity demanded by the task. This can be solved for every time point to define the null-space activity. This method means that for any given potent activity, there is a unique set of null activity. This is physiologically implausible, so variability was incorporated by sampling from a Poisson distribution

parameterised by the solution to the quadratic programming problem: $\hat{\mathbf{x}} \sim \text{Poisson}(\mathbf{x})$.

With the null-activity defined, the same process of splitting the potent activity into quadrants and plotting the null-space activity was performed. Figure 34 shows the same exemplar quadrant as previously, this time showing the null-firing rates distributed according to the minimal-firing hypothesis.

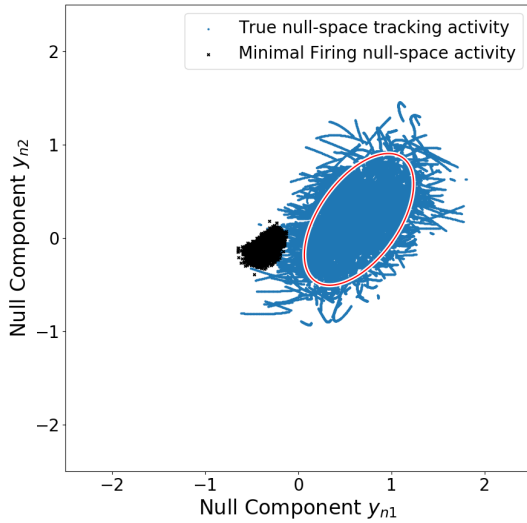


Figure 34: Distribution of first two components of null-space activity according to Minimal Firing Hypothesis

We see that there is very little agreement between the firing rates distributed according to the minimal firing hypothesis and the actual samples. The minimal firing hypothesis tries to keep the null-space activity as close to zero as possible, however we see that the tracking data has significantly greater vari-

ance. This observation is consistent for all quadrants, as we see in Figure 35.

5.5 Quantitative Comparison of Distributions

With the different models of null-activity completed, we now assess the fit with the true null-space activity. While it is possible to make qualitative observations as to how well each model fits the data, a quantitative measure would be preferred.

5.5.1 KL Divergence of Multivariate Gaussians

The Kullback-Leibler (KL) divergence quantifies the amount of difference between the two distributions. It can be used to compare the samples created by each model and the true null-space activity. This gives us a metric that allows comparison of different hypotheses. Identical distributions have a KL divergence of 0, so the observations made above would indicate that the KL divergence of the samples drawn from the conditional distribution should be lower than that of the shuffled activity and that generated by the minimal firing hypothesis.

For continuous random variables, the KL Divergence is defined as

$$D_{KL}(P||Q) = \int_{-\infty}^{\infty} p(x) \log \left(\frac{p(x)}{q(x)} \right) dx \quad (56)$$

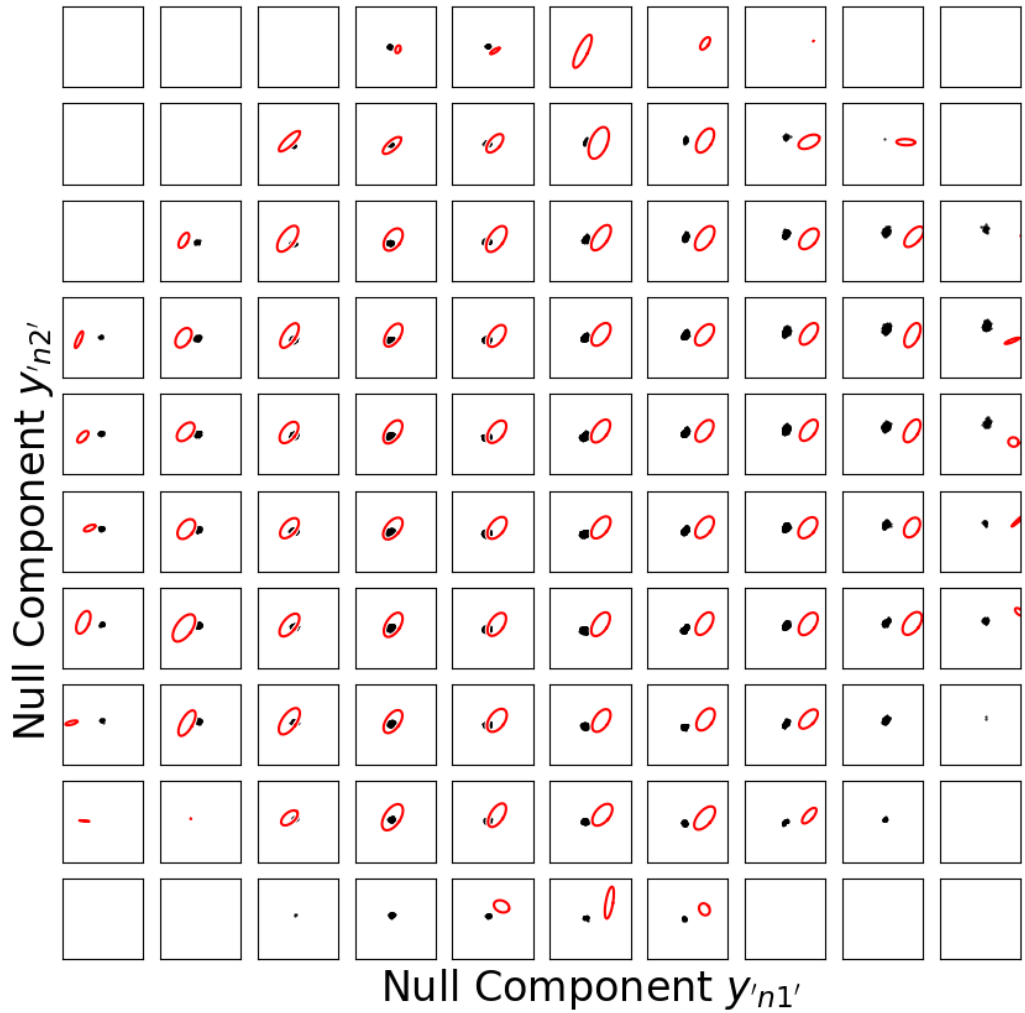


Figure 35: Top two components of null space activity generated by the minimal firing hypothesis compared with the 2σ contour of the true activity

We model the samples as a k-dimensional multivariate normal distribution with pdf

$$p(x) = (2\pi)^{-\frac{k}{2}} \det(\Sigma)^{-\frac{1}{2}} e^{-\frac{1}{2}(x-\mu)^T \Sigma^{-1} (x-\mu)} \quad (57)$$

while the theoretical conditional distribution is also a multivariate normal with mean and variance as found in Section 5.4.1. Substituting into (56) gives the KL divergence of two multivariate Gaussians.

$$D_{KL}(P||Q) = \frac{1}{2} [\log \frac{|\Sigma_2|}{|\Sigma_1|} - k + (\mu_1 - \mu_2)^T \Sigma_2^{-1} (\mu_1 - \mu_2) + \text{tr}\{\Sigma_2^{-1} \Sigma_1\}] \quad (58)$$

The full derivation can be found in Appendix C.

5.5.2 KL Divergence of the different models of null-space activity

If we model all the distributions as gaussians, Equation 58 can be used to give a quantitative measure of fit for the different distributions of null-space activity. Figure 36 shows the KL divergence calculated for each quadrant and plotted against the quadrant number (the gaps are due to the fact that some quadrants don't contain any data). We see that KL divergence of the true null-space activity is significantly lower than that of the shuffled null-space activity, confirming the qualitative observations made that the agreement was less accurate. Some periodicity is observed, as the quadrants at the edges of the distribution

agree less well due to the edge effects of the distribution of potent activity.

5.6 Discussion

We see from these results that the fixed distribution hypothesis arises naturally from the network model of M1 dynamics. The underlying, joint distribution of firing rates is set by the co-modulation patterns of the network, and so regardless of the choice of control space, the null-space activity remains coupled to the output-potent activity. The model behaves as described by Kao (4), with the network interactions shaping the response of the activity patterns and confining the activity to some fixed repertoire. While using the principle of minimum energy is useful for resolving muscular redundancy, it is clear that the minimal firing hypothesis does not accurately describe the data collected.

5.7 Summary

Neural redundancy can have many computational uses, for example in the act of preparing for movement. In this section, the BCI model was used to test observations made by Hennig et al. regarding the distribution of activity in the output-null dimensions. Their findings suggested that output-potent activity and output-null activity are coupled, such that when the task demands fix the output-potent

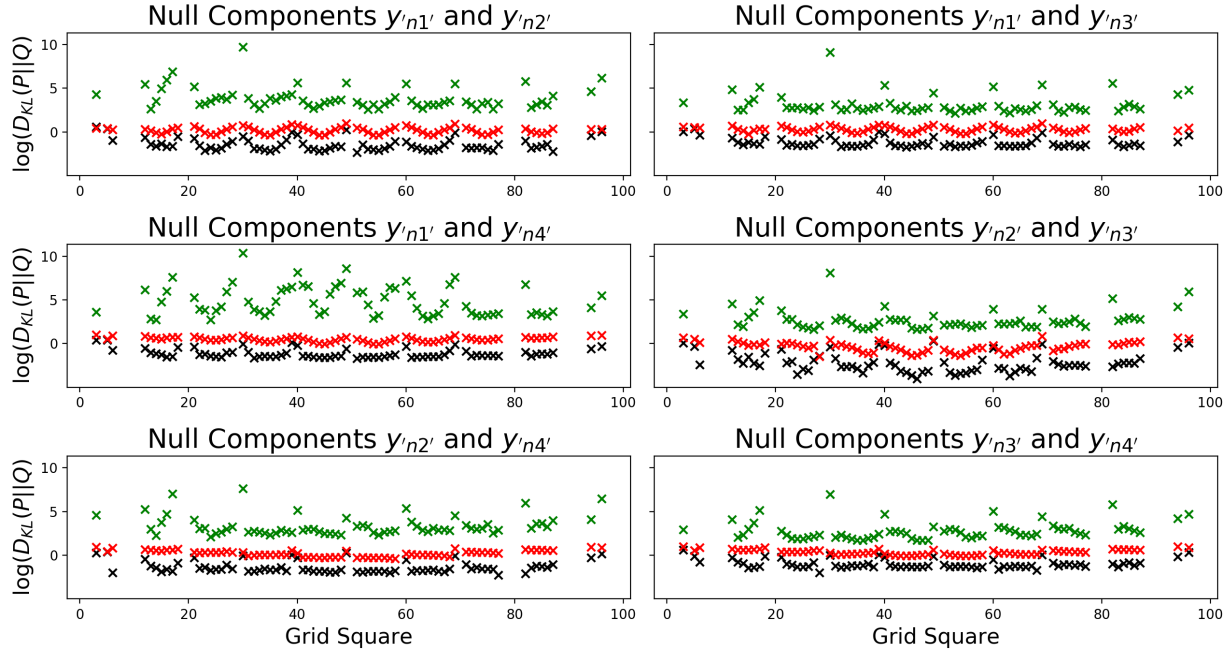


Figure 36: KL divergences for each quadrant for different components of null-space activity.
 Black: Fixed Distribution Hypothesis. Red: Shuffled Null-space components. Green: Minimal Firing Hypothesis

activity, there are constraints on the variability in output-null activity. We see from the results that the distribution of null-activity for given output-potent activity generated by the model agreed best with theoretical samples generated through conditioning on the output-potent activity. Minimum energy principles failed to explain the null-activity generated by the model, indicating that neural redundancy is resolved differently to muscular redundancy.

6 Conclusion

The aim of this project was to use a model of cortical dynamics to investigate two em-

pirical phenomena observed during a BCI task-learning experiment. It was found that the observation by Sadtler that the ability of the monkeys to relearn the task under control space perturbations was strongly dependent on the alignment of the control space with the controllability gramian of the system. The less well aligned they are, the more energy is required to perform the task. Thus, assuming control inputs to M1 to be energy-limited (as robustness demands), this property manifests itself in the monkey not being able to perform the task as successfully.

The optimal tracking paradigm was then used to investigate the distribution of null-space activity. It was found that to fit the data gener-

ated by the optimal tracking most accurately, samples should be drawn from a multivariate normal distribution conditioned on the output-potent activity. We see that the fixed distribution is the joint distribution of all neural activity, independent of choice of control space. Once the control space is set, the output-null activity is constrained by the output-potent activity demanded by the task.

7 Further Work

In the paper by Hennig et al., they compared 7 different methods of predicting null-space activity, of which the minimal firing hypothesis and the fixed distribution hypothesis are two. While the fixed distribution hypothesis agrees well with the data, it would be beneficial to test the other five methods in order to be sure that the fixed distribution hypothesis is indeed the best.

Subsequently, different models of M1 dynamics could be used to perform the same simulations. The results presented here provide evidence that the model of M1 developed by Kao et al. is an accurate representation of dynamics in the motor cortex, however the simulations described above would allow direct comparison of different models.

A Derivation of Lyapunov Equation from Stochastic Differential Equation

Consider the stochastic differential equation:

$$\dot{\mathbf{x}} = \mathbf{A}\mathbf{x} + \mathbf{B}dW. \quad (59)$$

Assume the white noise is distributed normally with zero mean and unit variance. Then, in discrete time

$$\mathbf{x}(t + \delta t) = \mathbf{x}(t) + \mathbf{A}\mathbf{x}(t)\delta t + \mathbf{B} * \frac{\mathcal{N}(\mathbf{0}, \mathbf{I})}{\sqrt{\delta t}} * \delta t$$

Now, post-multiply by its transpose.

$$\begin{aligned} \mathbf{x}(t + \delta t)\mathbf{x}(t + \delta t)^T &= (\mathbf{x}(t) + \mathbf{A}\mathbf{x}(t)\delta t + \mathbf{B}\sqrt{\delta t} * \mathcal{N}(\mathbf{0}, \mathbf{I}))(\mathbf{x}(t) + \mathbf{A}\mathbf{x}(t)\delta t + \mathbf{B}\sqrt{\delta t} * \mathcal{N}(\mathbf{0}, \mathbf{I}))^T \\ \mathbf{x}(t + \delta t)\mathbf{x}(t + \delta t)^T &= \mathbf{x}(t)\mathbf{x}(t)^T + \mathbf{A}\mathbf{x}(t)\mathbf{x}(t)^T \mathbf{A}^T \delta t^2 + \mathbf{B}\mathcal{N}(\mathbf{0}, \mathbf{I})\mathcal{N}(\mathbf{0}, \mathbf{I})^T \mathbf{B}^T \delta t + \\ &\quad \mathbf{x}(t)\mathbf{x}(t)^T \mathbf{A}^T \delta t + \mathbf{A}\mathbf{x}(t)\mathbf{x}(t)^T \delta t + \text{cross terms} \end{aligned}$$

Now take the expectation, and define $\mathbb{E} [\mathbf{x}(t)\mathbf{x}(t)^T] = \mathbf{P}(t)$, where $\mathbf{P}(t)$ is the covariance matrix at time t . By definition of white noise, the expectation of the cross terms is zero.

$$\begin{aligned} \mathbf{P}(t + \delta t) &= \mathbf{P}(t) + \mathbf{A}\mathbf{P}(t)\mathbf{A}^T \delta t^2 + \mathbf{B}\mathbf{B}^T \delta t + \mathbf{P}(t)\mathbf{A}^T \delta t + \mathbf{A}\mathbf{P}(t)\delta t \\ \frac{\mathbf{P}(t + \delta t) - \mathbf{P}(t)}{\delta t} &= \mathbf{A}\mathbf{P}(t)\mathbf{A}^T \delta t + \mathbf{B}\mathbf{B}^T + \mathbf{P}(t)\mathbf{A}^T + \mathbf{A}\mathbf{P}(t) \end{aligned}$$

Take the limit as $dt \rightarrow 0$:

$$\frac{d\mathbf{P}}{dt} = \mathbf{A}\mathbf{P} + \mathbf{P}\mathbf{A}^T + \mathbf{B}\mathbf{B}^T \quad (60)$$

At steady state, $\dot{\mathbf{P}} = 0$, so

$$0 = \mathbf{A}\mathbf{P} + \mathbf{P}\mathbf{A}^T + \mathbf{B}\mathbf{B}^T \quad (61)$$

This is the desired Lyapunov equation.

B Comparison of different null-space components

Figures 37 and 38 shows the distribution of the second and third null components for the true data and the shuffled data compared with the gaussian contours of the conditional distribution.

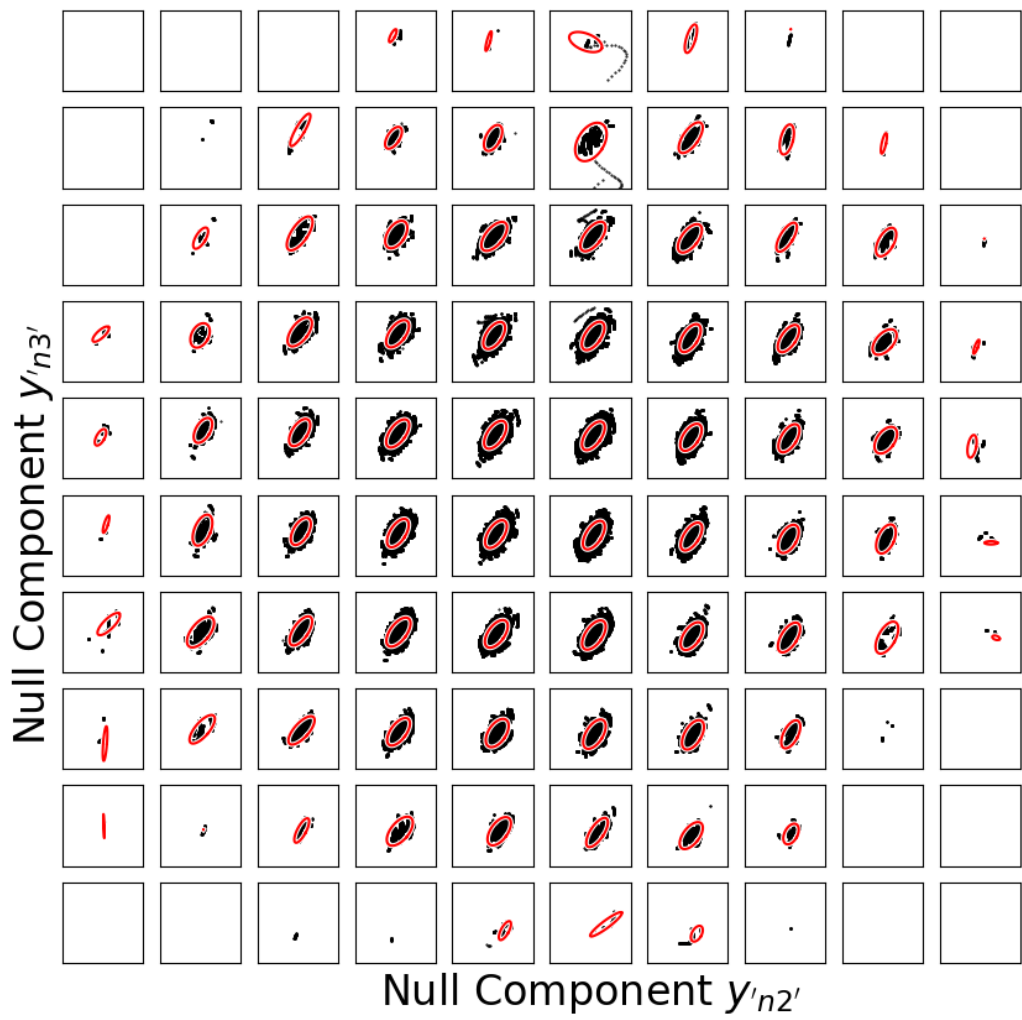


Figure 37: Second and third true null components

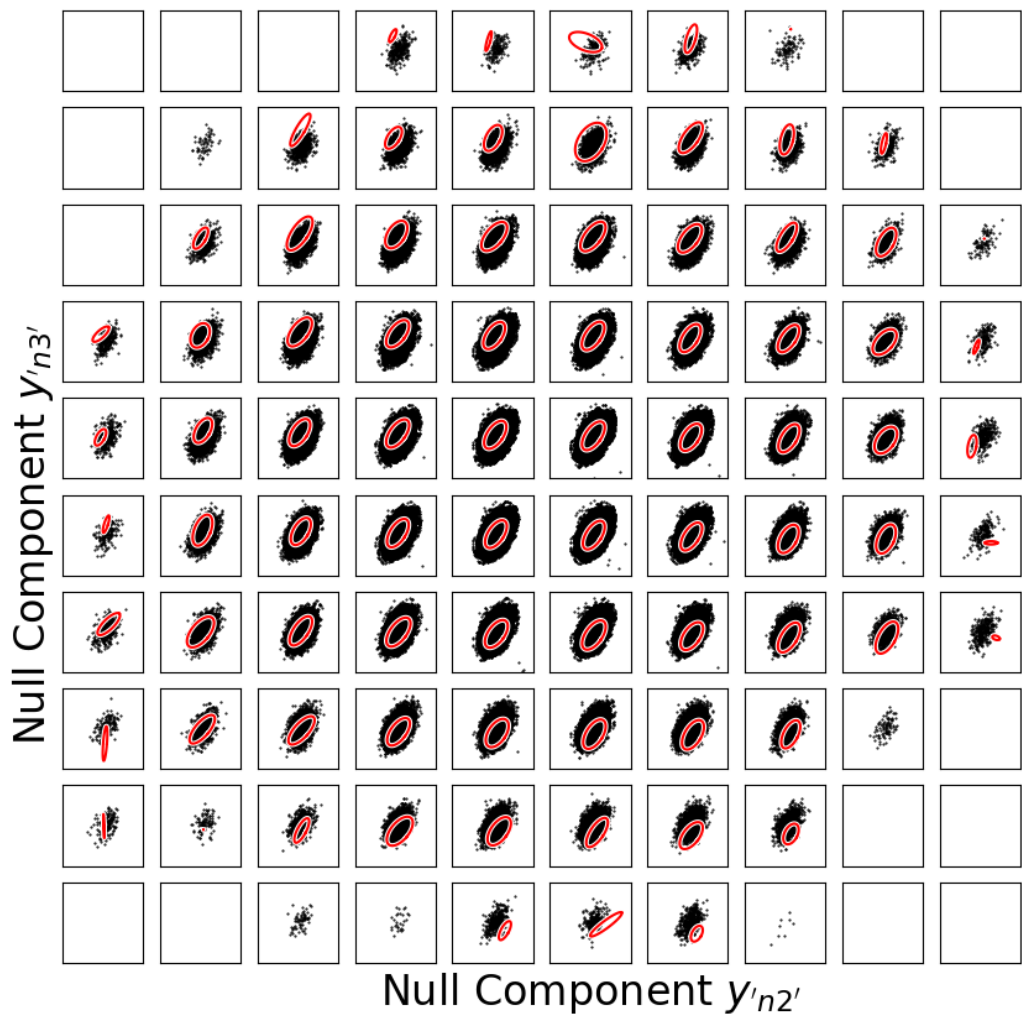


Figure 38: Second and third shuffled null components

C Derivation of KL Divergence of Multivariate Gaussians

The KL divergence of two multivariate Gaussians can be derived as follows

$$\begin{aligned} D_{KL}(P||Q) &= \int_{-\infty}^{\infty} p(x) \log \left(\frac{p(x)}{q(x)} \right) dx \\ &= \int_{-\infty}^{\infty} \left[\frac{1}{2} \log \frac{|\Sigma_2|}{|\Sigma_1|} - \frac{1}{2} (x - \mu_1)^T \Sigma_1^{-1} (x - \mu_1) + \frac{1}{2} (x - \mu_2)^T \Sigma_2^{-1} (x - \mu_2) \right] p(x) dx \\ &= \frac{1}{2} \left[\log \frac{|\Sigma_2|}{|\Sigma_1|} - \mathbb{E} [(x - \mu_1)^T (x - \mu_1) \Sigma_1^{-1}] + \mathbb{E} [(x - \mu_2)^T (x - \mu_2) \Sigma_2^{-1}] \right] \\ &= \frac{1}{2} \left[\log \frac{|\Sigma_2|}{|\Sigma_1|} - \text{tr}\{I_k\} + (\mu_1 - \mu_2)^T \Sigma_2^{-1} (\mu_1 - \mu_2) + \text{tr}\{\Sigma_2^{-1} \Sigma_1\} \right] \\ &= \frac{1}{2} \left[\log \frac{|\Sigma_2|}{|\Sigma_1|} - k + (\mu_1 - \mu_2)^T \Sigma_2^{-1} (\mu_1 - \mu_2) + \text{tr}\{\Sigma_2^{-1} \Sigma_1\} \right] \end{aligned}$$

using properties from section 8.2 of the Matrix Cookbook (9)

D Risk Assessment Retrospective

This project was purely a software project and so no hazards were encountered.

References

- [1] Sadtler, P., Quick, K., Golub, M. et al. Neural constraints on learning. *Nature* 512, 423–426 (2014). <https://doi.org/10.1038/nature13665>
- [2] Hennig, J.A., Golub, M.D., Lund, P.J., Sadtler, P.T., Oby, E.R., Quick, K.M., Ryu, S.I., Tyler-Kabara, E.C., Batista, A.P., Byron, M.Y. and Chase, S.M., 2018. Constraints on neural redundancy. *Elife*, 7, p.e36774.
- [3] Kaufman, M., Churchland, M., Ryu, S. et al. Cortical activity in the null space: permitting preparation without movement. *Nat Neurosci* 17, 440–448 (2014). <https://doi.org/10.1038/nn.3643>
- [4] Kao T-C., Hennequin G., 2018. Null ain't dull: New perspectives on motor cortex. *Trends in Cognitive Sciences*
- [5] Churchland, M., Cunningham, J., Kaufman, M. et al. Neural population dynamics during reaching. *Nature* 487, 51–56 (2012). <https://doi.org/10.1038/nature11129>

- [6] Kao T-C., Sadabadi S. M., Hennequin G., Optimal anticipatory control of movement as a theory of motor preparation: a thalamo-cortical circuit model, (2019). bioRxiv 2020.02.02.931246; doi: <https://doi.org/10.1101/2020.02.02.931246>
- [7] Li, W. and Todorov, E., 2004, August. Iterative linear quadratic regulator design for nonlinear biological movement systems. In ICINCO (1) (pp. 222-229).
- [8] Bryson, A.E., 1999. Dynamic Optimisation. Addison Wesley Longman, Inc.
- [9] Pederson, M. S., Peterson, K.B., 2012, The matrix cookbook.
<https://www.math.uwaterloo.ca/~hwolkowi/matrixcookbook.pdf>